Combustion and Flame 162 (2015) 315–330

Contents lists available at ScienceDirect

Combustion and Flame

journal homepage: www.elsevier.com/locate/combustflame

An ignition delay and kinetic modeling study of methane, dimethyl ether, and their mixtures at high pressures

Ultan Burke [a], Kieran P. Somers [a], Peter O'Toole [a], Chis M. Zinner [c], Nicolas Marquet [c], Gilles Bourque [b], Eric L. Petersen [c], Wayne K. Metcalfe [a], Zeynep Serinyel [a], Henry J. Curran [a,*]

[a] Combustion Chemistry Centre, NUI Galway, Ireland
[b] Rolls-Royce Canada, Montreal, QC H8T 1A2, Canada
[c] Department of Mechanical Engineering, Texas A&M University, College Station, TX, USA

ARTICLE INFO

Article history:
Received 12 June 2014
Received in revised form 20 August 2014
Accepted 21 August 2014
Available online 29 September 2014

Keywords:
Shock tube
Rapid compression machine
Methane
Dimethyl ether
Ignition delay times
High pressure

ABSTRACT

The development of accurate chemical kinetic models capable of predicting the combustion of methane and dimethyl ether in common combustion environments such as compression ignition engines and gas turbines is important as it provides valuable data and understanding of these fuels under conditions that are difficult and expensive to study in the real combustors. In *this work*, both experimental and chemical kinetic model-predicted ignition delay time data are provided covering a range of conditions relevant to gas turbine environments (T = 600–1600 K, p = 7–41 atm, ϕ = 0.3, 0.5, 1.0, and 2.0 in 'air' mixtures). The detailed chemical kinetic model (Mech_56.54) is capable of accurately predicting this wide range of data, and it is the first mechanism to incorporate high-level rate constant measurements and calculations where available for the reactions of DME. This mechanism is also the first to apply a pressure-dependent treatment to the low-temperature reactions of DME. It has been validated using available literature data including flow reactor, jet-stirred reactor, shock-tube ignition delay times, shock-tube speciation, flame speed, and flame speciation data. New ignition delay time measurements are presented for methane, dimethyl ether, and their mixtures; these data were obtained using three different shock tubes and a rapid compression machine. In addition to the DME/CH_4 blends, high-pressure data for pure DME and pure methane were also obtained. Where possible, the new data were compared with existing data from the literature, with good agreement.

1. Introduction

The depletion of crude oil resources has motivated the search for alternative energy sources. Currently, the combustion of hydrocarbons remains the biggest producer of energy throughout the world, and in the short- to medium-term will remain so. However, the combustion of fossil fuels has contributed to global warming and increased levels of pollution. Biofuels can be produced from renewable sources and can reduce undesirable emissions associated with conventional fossil fuels. Methane (CH_4), which is the predominant component of natural gas, is a relatively clean-burning fossil fuel and can be considered a renewable energy source when produced as biomethane via anaerobic digestion of biomass [1]. Dimethyl ether (DME) is also considered a second generation biofuel as it can be produced from biomass. It is more commonly produced in a two-step process, where syngas is converted to methanol which can then be used to generate DME through a dehydration reaction [2]. Semelsburger et al. [3] found that DME ranks highly as an alternative fuel for the future.

It is for these reasons that a large number of studies have been performed on the combustion of these fuels. Due to its high cetane number (55), DME is considered a good alternative to diesel. DME has been studied experimentally in diesel engines [4–7] showing its advantages in terms of emissions and engine efficiency. Particulate matter (PM) emissions were found to be greatly reduced, as were NO_x and SO_x, while there was a slight increase in carbon monoxide (CO) and hydrocarbon (HC) emissions.

Methane is the main component of natural gas and is commonly burned in gas turbines. Due to DME's excellent autoignition characteristics, it has been used as an additive or alternative to natural gas in gas turbines [8,9], leading to interest in the combustion kinetics of mixtures of these two fuels. Mixtures of methane and DME have also been studied within homogeneous

* Corresponding author. Address: Combustion Chemistry Centre, School of Chemistry, NUI Galway, Ireland.
E-mail address: henry.curran@nuigalway.ie (H.J. Curran).
URL: http://c3.nuigalway.ie/ (H.J. Curran).

http://dx.doi.org/10.1016/j.combustflame.2014.08.014
0010-2180/

charge compression ignition (HCCI) engines [10,11], where DME was found to be an excellent ignition improver. Several flame speed studies have been conducted on DME [12–17] using a variety of different methods such as constant-volume bomb using optical observation of the flame and counterflow flames; in some devices, particle image velocimetry has been utilized to determine the laminar flame speed from the observed gas velocities.

Species profiles were first measured by Dagaut et al. [18] in a jet-stirred reactor (JSR) using fuel mixtures highly diluted in argon, for equivalence ratios from 0.2 to 1.0, at a pressure of 10 atm, and in the temperature range 550–1100 K. Subsequently, flow-reactor data were taken by Fischer et al. [19] (1118 K, 3.5 atm, and 1085 K, 1 atm, $\phi = 0.32–3.40$) and Curran et al. [20] (550–850 K, 12–18 atm, $\phi = 0.7–4.2$). These studies [19,20] also developed a detailed chemical kinetic mechanism to simulate their experimental data, using it to identify the important reaction pathways controlling DME fuel oxidation. This mechanism was also used to simulate JSR data [18] and shock-tube ignition delay times.

Zhao et al. [21] used Rice–Ramsperger–Kassel–Marcus (RRKM)/master equation calculations to calculate rate constants for the unimolecular decomposition of DME as a function of temperature and pressure. Their study also reported flow reactor data at 980 K and 10 atm as a function of residence time. A chemical kinetic model was validated using experimental data which included flow reactor, JSR, shock tube ignition delays, laminar flame speciation and flame speed measurements. Wang et al. [22] and Cool et al. [23] used electron–ionization molecular-beam mass spectrometry and photoionization molecular-beam mass spectrometry performed using synchrotron radiation for the analysis of a stabilized flat flame to provide species profiles within DME flames.

Cook et al. [24] used laser absorption of ȮH radicals behind reflected shock waves to isolate and measure the rate constants of the decomposition of DME and the rate constant for H-atom abstraction from DME by ȮH radicals at high temperatures. These measurements were coupled with RRKM/master equation calculations which agreed well with the measurements. Recently, Pyun et al. [25] measured species profiles for CO, CH_4, and C_2H_4, during the pyrolysis of DME within a shock tube using tunable laser absorption with a quantum cascade laser. This laser absorption study was done at a range of reflected-shock temperatures (1300–1600 K) and at a reflected-shock pressure of 1.5 atm.

Previous ignition delay time studies of these fuels and their mixtures are summarized in Tables 1 and 2. These studies cover a wide range of conditions including low-to-high temperatures and pressures. Of these previous ignition delay time studies [26–37], only the work of Tang et al. [37] included mixtures of CH_4 and DME. It covered dilute mixtures within a pressure range of 1–10 atm. The current study covers a wider range of temperatures and pressures and includes fuel in 'air' mixtures.

Recent experimental studies of DME combustion also include a flame speed and flame speciation study by Liu et al. [38]. The effect of diluting DME flames with 20% CO_2 was studied, and flame speeds over a range of pressures were reported. Flame speciation using electron–ionization molecular-beam mass spectrometry was measured. Guo et al. [39] measured low temperature species profiles in an atmospheric flow reactor with electron–ionization molecular-beam mass spectrometry used as the detection system. Herrmann et al. [40] used an atmospheric flow reactor to measure mole fractions of species related to DME oxidation at low temperatures (400–1200 K) by time-of-flight mass spectrometry. Both of these studies compared their measured data to models available in the literature.

In *this study*, we provide new ignition delay time data for these two important fuels over wide regimes of temperature and pressure at engine- and turbine-relevant conditions. We have developed a detailed chemical kinetic mechanism (Mech_56.54) based on the widely validated mechanism AramcoMech1.3 [41], which is capable of predicting these new ignition delay data and available literature data. Presented first is an overview of the experiments, including details on the mixtures studied, the facilities, the measurement techniques, and modeling approaches. The experimental section is followed by a summary of the chemical kinetic mechanism and the reaction rates that were modified for the present study. A results and discussion section comprises the bulk of this paper and presents all of the ignition delay time data as well as comparisons to the kinetic mechanism. Sensitivity analyses and relevant discussions on the observed trends are also provided.

Table 1
CH_4 ignition delay time studies from the literature.

Instrument	Mixture	p (atm)	T (K)	Year	Reference
Review				1994	[26]
Shock tube	Dilute in Ar	3–300	1800	1974	[27]
Shock tube	Dilute in Ar	9–480	1410–2040	1996	[28]
Shock tube	Fuel-rich	35–260	1040–1600	1999	[29,30]
RCM	'Air'	13–16	980–1060	2001	[31]
Shock tube	Fuel-lean	3–450	1200–1700	2003	[32]
Shock tube	'Air'	16–40	1000–1350	2004	[33]

Table 2
Summary of DME ignition delay time studies from the literature.

Instrument	Mixture	p (atm)	T (K)	Year	Reference
RCM	'Air'	9.87–19.74	615–735	2008	[34]
Shock tube	'Air'	12.83–39.48	662–1266	1996	[35]
Shock tube	Dilute in Ar	1.58–6.51	1175–1900	2009	[36]
Shock tube	Dilute in Ar	1.00–9.87	1134–2105	2012	[37]

2. Experimental

A common set of mixtures was selected for study in both the rapid compression machine (RCM) and in the shock tubes, Table 3.

For the experiments at NUIG, methane and DME gases were obtained from Sigma–Aldrich at ⩾99.0% and ⩾99.9% purity respectively, while all other gases were supplied by BOC Ireland; nitrogen (CP Grade) ⩾99.95%, argon (Research Grade) ⩾99.9995%, oxygen (Medical Grade) ⩾99.5% and all were used without further purification. At TAMU, the DME was Grade 2.6 purity (99.6%), the methane was Grade 3.7 (99.97%), and both the O_2

Table 3
CH_4/DME mixture compositions (%molar volume) tested in the present study.

	Mix No.	% CH_4	% CH_3OCH_3	% O_2	% Diluent	ϕ
100% CH_4	1	3.055	0.000	20.367	76.578	0.3
	2	4.990	0.000	19.960	75.050	0.5
	3	9.506	0.000	19.011	71.483	1.0
	4	17.361	0.000	17.361	65.278	2.0
CH_4/DME 80%/20%	5	2.228	0.557	20.423	76.792	0.3
	6	3.646	0.911	20.051	75.392	0.5
	7	6.974	1.743	19.177	72.106	1.0
	8	12.829	3.207	17.640	66.324	2.0
CH_4/DME 60%/40%	9	1.535	1.024	20.471	76.970	0.3
	10	2.516	1.677	20.127	75.680	0.5
	11	4.829	3.220	19.317	72.634	1.0
	12	8.939	5.959	17.878	67.224	2.0
100% DME	13	0.000	2.058	20.576	77.366	0.3
	14	0.000	3.383	20.298	76.319	0.5
	15	0.000	6.545	19.634	73.821	1.0
	16	0.000	12.285	18.428	69.287	2.0

and N_2 were ultra high purity grade (99.999%). All test mixtures were made in stainless steel mixing vessels using partial pressures to determine the volumetric percentage of each constituent to within 1% of their reported value. The N_2 and O_2 were mixed in the ratio of 3.76–1. Test mixtures were allowed to mix for at least 4 h before use. For the Texas A&M University (TAMU) shock-tube mixing tanks, the gases were introduced into the mixing tanks through a perforated tube that extended the length of the mixing chamber, inducing turbulent mixing.

2.1. Rapid compression machine

The heated rapid compression machine used here has been described in detail by Brett et al. [31] and Affleck et al. [42]. It has a twin opposed piston configuration. The heating system has been described by Darcy et al. [43]. Pressure profiles are recorded using a pressure transducer (Kistler 603B) with the signal passing through a charge amplifier and recorded on a digital oscilloscope. Experimental compression times are quite short at approximately 16 ms. The ignition delay time, τ_{ign}, was defined as the time from the end of compression to the maximum rate of pressure rise as shown in Fig. 1. Compressed pressures and ignition delay times were reproducible to within 15% at each compressed temperature (T_c). The initial and compressed pressure and temperature along with the ignition delay time measurements for all experiments are provided as Supplementary Material.

The compressed gas temperature, T_c, was calculated from the initial temperature, T_i, initial pressure, p_i, reactant composition, and the experimentally measured compressed gas pressure, p_c. The compressed gas pressure is defined as the first local maximum on the pressure profile, and frozen chemistry was assumed during compression. The temperature calculation employed the adiabatic compression/expansion routine in Gaseq [44] which uses the temperature dependence of the ratio of specific heats, γ, according to:

$$\ln\left(\frac{p_c}{p_i}\right) = \int_{T_i}^{T_c} \frac{\gamma}{\gamma - 1}\frac{dT}{T}$$

2.2. Shock tubes

Three different shock-tube facilities were used in this study. The first is located at NUI Galway (NUIG). It is an updated version of the shock tube described in detail by Darcy et al. [45]. It has an inner diameter of 6.35 cm, a driver section 3 m in length which is separated from the driven section (5.7 m in length) by a double diaphragm section (3 cm in length) which houses two pre-scored aluminum diaphragms per experiment. It has been updated to increase the range of reflected-shock pressures that can be safely achieved and to increase the level of accuracy in the shock velocity measurement by employing an extra PCB113A pressure transducer which provides a fifth shock velocity measurement. This facility was used to obtain ignition delay time measurements from 1.0 to 5.5 ms using tailored interface conditions. This method entails the addition of nitrogen to helium driver gas by tailoring the acoustic impedance such that the interaction between the reflected shock and the contact surface results in the flow velocity of the contact surface becoming near static and there is no further interaction of the reflected shock wave with the test gas. Conditions for the tailored-interface shock-tube experiments were determined using an in-house shock code based on the normal, 1-D shock wave relations.

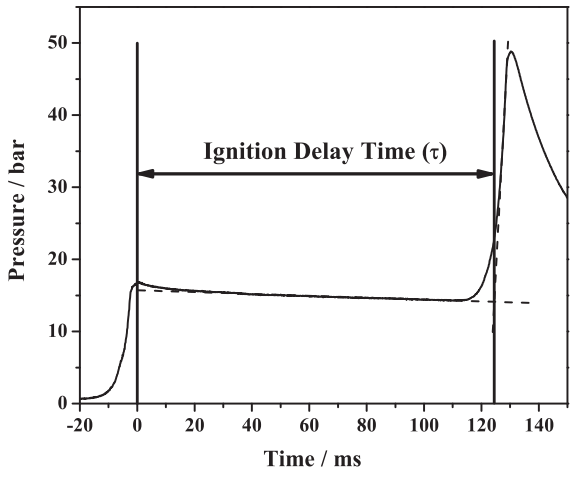

Fig. 1. Typical pressure trace used to determine ignition delay time for a $\phi = 2.0$ mixture of 60% CH_4/40% DME in 'air' at $p_i = 0.661$ atm, $T_i = 314$ K, $p_c = 16.8$ atm, $T_c = 647.0$ K, $\tau_{ign} = 129.6$ ms.

The NUIG shock tube is equipped with PCB 113A and Kistler 603B pressure transducers at the sidewall and endwall, respectively, to determine ignition delay measurements from the sharp increase in pressure due to ignition for the undiluted fuel–air mixtures studied herein.

The other two shock-tube facilities were operated by the TAMU authors, the first of which has been described previously by Petersen et al. [46]. It is constructed of stainless steel 304 with a 10.7 m long driven section and an internal diameter of 16.2 cm. The driver section is 3.5 m long and has an internal diameter of 7.62 cm. The second TAMU facility is described in Aul et al. [47]. This facility has a driven-section inner diameter of 15.24 cm with a length of 4.72 m. Its driver section has a 7.62-cm inner diameter and is 2.46 m long. In both shock tubes, the incident-shock velocity profile along the driven-section tube is recorded by five PCB 113A pressure transducers triggering four Fluke PM 6666 time interval counters. The resulting profile was extrapolated to the endwall to obtain the reflected-shock conditions at the endwall using the 1-D, normal shock relations and the Sandia thermodynamic database. This method results in a reflected-shock temperature uncertainty of 10 K at time zero [46].

For both facilities, the relatively large diameters (greater than 15 cm) led to minimal facility-induced, post-shock pressure increases [48]. The typical boundary-layer-induced dp/dt near the endwall region was 2%/ms or less. In addition, any facility-induced pressure effect was overshadowed by the (albeit slight) first-stage pressure rise due to the early DME reaction. The pressure at the endwall from which the ignition delay time was inferred was obtained from a PCB 134A transducer in both facilities, and the sidewall pressure (1.6 cm from the endwall in both tubes) was monitored via a Kistler 603B1 transducer. As shown in Fig. 2, the primary ignition event was rather clear from the sharp increase in pressure, and for all experiments the endwall pressure was used to determine the ignition delay time; the sidewall pressure measurements served to confirm the timing of the main ignition event. Pre-scored aluminum diaphragms in a single-diaphragm configuration were used for the TAMU experiments.

In addition to pressure, the emission from excited-state species was also monitored in all experiments through either CaF_2 or sapphire windows at both the endwall and sidewall (1.6 cm from endwall) locations in both TAMU shock tubes. The experiments in the Petersen et al. [46] shock tube monitored CH^* chemiluminescence through a 430-nm narrowband (10 nm) filter, while the tests in the Aul et al. [47] facility utilized OH^* through a 307-nm narrowband filter. Photomultiplier tubes from Hamamatsu (1P21) were used to record the light emission through home-made housings and electronics. In all cases, the light emission confirmed the results from the pressure traces. The slight increase in pressure

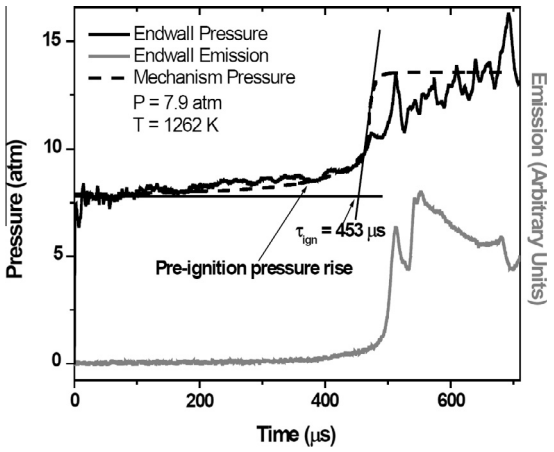

Fig. 2. Typical endwall, pressure and CH^* emission traces used to determine ignition delay time for a $\phi = 0.3$ in 'air' mixture of 60% CH_4/40% DME at T_5 = 1262 K, p_5 = 7.9 atm, τ_{ign} = 453 μs.

prior to the main ignition event (due to a first-stage ignition) was also detected in the chemiluminescence signals. It should be noted that this first-stage reaction is reproduced quite well by the chemical kinetic model (described below), which is able to capture the increase in pressure prior to the main ignition event. More discussion on the first-stage pressure rise and the ignition delay times from the CH_4/DME blends is contained in the M.S. thesis by Zinner [49]. Most the results for the pure DME and CH_4 experiments were presented in the conference paper by Pemelton et al. [50].

For the real fuel/air mixtures utilized in this study, significant pressure rises are associated with combustion. Therefore, ignition delay times were determined by measuring the pressure rise at the endwall for the shock-tube experiments. Endwall emission traces from the activated complex CH^* were also used to provide qualitative results for comparison. Example pressure and emission traces are provided in Fig. 2. In most cases, the pressure rise due to the ignition event was quite rapid, so the ignition time was clear. In some experiments, such as the one shown in Fig. 2, the CH^* (or OH^*) emission measurement served as a guide for the selection of the main ignition event in the pressure trace. More examples of pressure traces are provided as Supplementary Material. Chemiluminescence from OH^* produced emission traces similar to the one shown in Fig. 2.

3. Computational modeling

ChemkinPRO [51] was used for all simulations. Two methods of simulation were used to model the shock tube and RCM data and are discussed here.

3.1. RCM simulation

Roll-up vortices can cause temperature gradients within the combustion chamber due to the entrainment of the cold boundary layer from the walls into the chamber. This effect is minimized by using piston heads which have crevices to capture the boundary layer and whose dimensions are optimized for the conditions of our RCM leading to a good spatial temperature homogeneity in the combustion chamber as predicted by Würmel et al. [52] using CFD simulations.

Due to the long residence times in the RCM, it is necessary to account for heat losses during experiments, which occur mainly via diffusion of the core test gas to the relatively cold walls of the combustion chamber. This effect is accounted for by performing non-reactive experiments concurrently with reactive experiments. These unreactive experiments are performed by replacing molecular oxygen with nitrogen as they have similar heat capacities and thermal diffusivities. The pressure–time profiles from these non-reactive experiments are converted to volume-time profiles. These profiles are included in our simulations to account for the pressure and temperature change in the test mixture during experiment. Once these facility effects have been accounted for, the RCM is simulated as a homogeneous batch reactor with varying volume.

3.2. Shock-tube simulation

Shock-tube experiments are commonly simulated assuming either constant-volume or constant-pressure conditions. The short residence times associated with conventional shock tubes means that they can generally be assumed to be adiabatic reactors. For ignition delay times greater than 1000 μs and in particular for high pressures as discussed by Petersen [53], it may be necessary to account for non-ideal effects to accurately simulate the data. This scenario depends on the extent of the pressure/temperature change during experiments.

In this study, the shock tubes were simulated as constant-volume, homogeneous batch reactors. It was necessary to account for a linear pressure increase due to non-ideal effects in some cases, in particular for the NUIG experiments with ignition delay times longer than about 1 ms for pure methane. These effects were accounted for by including a volume profile to account for the change of pressure and temperature with time, similar to the RCM simulation described above. By quantifying the rate of pressure rise, excluding pressure rise due to ignition, a facility effect pressure profile for a given experiment could be incorporated into our simulations.

3.3. Sensitivity and flux analyses

Brute-force sensitivity analyses were carried out to identify the important reactions controlling ignition under our experimental conditions. Sensitivity coefficients (S) were determined using the equation:

$$S = \frac{\ln(\tau_+/\tau_-)}{\ln(k_+/k_-)} = \frac{\ln(\tau_+/\tau_-)}{\ln(2.0/0.5)}$$

Negative sensitivity coefficients denote a promoting effect (decreasing ignition delay time when a rate constant is increased), while a positive coefficient points to an inhibiting effect (increasing ignition delay times when a rate constant is increased). Flux analyses were also performed to monitor the consumption and production of species under the experimental conditions of interest. All flux analyses were taken at the point of 20% fuel consumption. These analyses provide an understanding of the reactions and associated rate constants that control the predictions of the ignition delay times.

4. Chemical kinetic model

The present model (Mech_56.54) consists of the H_2/CO sub-mechanism of Kéromnès et al. [54], the C_1–C_2 base sub-mechanism of Metcalfe et al. [41] and the recently published propene mechanism of Burke et al. [55]. The data measured in this study and available literature data (JSR, flow reactor, RCM, shock tube, shock-tube speciation, flame speed, and flame speciation) have been used to re-validate the DME kinetic mechanism, Mech_56.54, developed here. The experimental data and the ChemkinPRO [51] format kinetics, thermodynamics, and transport properties files are

included as Supplementary Material. Also available are the ChemkinPRO [51] format input files for simulation of the RCM data, these can be found at http://c3.nuigalway.ie/ch4_dme.html. Provided in the following subsections are details on the thermodynamic data used and the rate constants that were used in the present version of the mechanism.

4.1. Thermodynamic data

The mechanism includes a re-evaluation of the thermodynamic properties for DME and the intermediate species relevant to its low-temperature combustion. The thermodynamic data were calculated using THERM [56] software which employed optimized group values [57] from comparison of available literature values. The study of Yamada et al. [58] provided thermodynamic calculations for key DME low-temperature radical intermediates ($CH_3OCH_2\dot{O}_2$ and $\dot{C}H_2OCH_2O_2H$). These calculations were used to optimize the group C/H_2/O/OO and the bond dissociation group CJOC. These groups were used in the calculation of the thermodynamic properties presented here and are provided as Supplementary Material.

4.2. Rate constants

Chemical kinetic rate constants were considered after finalizing the thermodynamic parameters. The rate constants altered relative to AramcoMech1.3 [41] relate exclusively to the DME sub-mechanism. These are presented and discussed in the following sections.

4.2.1. H-atom abstraction reactions

Rate constants for H-atom abstraction reactions were taken from the original work of Curran/Fischer et al. [19,20], with the exception of abstraction by $H\dot{O}_2, CH_3\dot{O}_2$ and $\dot{C}H_3$ radicals which have been altered in this study.

In previous mechanisms [19,21,41], the rate constant for H-atom abstraction by the hydroperoxyl radical was estimated using analogies to similar chemical systems. We use the rate constant from the recent quantum chemical calculations by Mendes et al. [59]. Table 4 lists comparisons of the rate constant used here with those from previously published models [19,21,41]. The rate constant used is approximately 50% slower than that used in the study of Curran/Fischer et al. [19,20] and AramcoMech1.3 [41], at temperatures between 700 and 1100 K. There is a factor of 3.8 difference at 1000 K in the rate constant used by Zhao et al. [21] and that calculated by Mendes et al., which has been employed here. It should be noted that the study of Zhao et al. [21] did not include the H-atom abstraction from the fuel by methylperoxyl radical which may explain why it was necessary for them to increase the rate of abstraction by hydroperoxyl radical.

The rate constant for H-atom abstraction by methylperoxyl radical used here is a factor of 2.5 lower than abstraction by hydroperoxyl radical which is a ratio based on the calculations of Carstensen and Dean [60]. Curran/Fischer et al. [19,20] used the same rate constant for abstraction by hydroperoxyl and methylperoxyl radicals.

The rate constant for H-atom abstraction by methyl radical is based on the measurements by Tranter et al. [61]. We have reduced their value by 45% which is within the uncertainty reported by the authors [61] as this improved agreement with the methane speciation profiles taken by Pyun et al. [25].

Table 4
Modified H-atom abstraction reactions. A, n and E_a in ChemkinPRO [51] format.

Reaction	Kinetic model	A	n	E_a
R1	*This Study*	3.17×10^{-03}	4.64	10556.0
	AramcoMech 1.3 [41]	$8.67 \times 10^{+02}$	3.01	12090.0
	Curran/Fischer et al. [19]	$1.68 \times 10^{+13}$	0.00	17690.0
	Zhao et al. [21]	$2.00 \times 10^{+13}$	0.00	16500.0
R2	*This Study*	1.27×10^{-03}	4.64	10556.0
	AramcoMech 1.3 [41]	$3.12 \times 10^{+02}$	3.12	13190.0
	Curran/Fischer et al. [19]	$1.68 \times 10^{+13}$	0.00	17690.0
R3	*This Study*	$7.02 \times 10^{+00}$	3.78	9687.0
	AramcoMech 1.3 [41]	1.45×10^{-06}	5.73	5700.0
	Curran/Fischer et al. [19]	1.45×10^{-06}	5.73	5700.0
	Zhao et al. [21]	$2.68 \times 10^{+01}$	3.78	9631.0

R1–$CH_3OCH_3 + H\dot{O}_2 \rightleftarrows CH_3O\dot{C}H_2 + H_2O_2$.
R2–$CH_3OCH_3 + CH_3\dot{O}_2 \rightleftarrows CH_3O\dot{C}H_2 + CH_3O_2H$.
R3–$CH_3OCH_3 + \dot{C}H_3 \rightleftarrows CH_3O\dot{C}H_2 + CH_4$.

4.2.2. Low temperature oxidation mechanism

The low-temperature DME oxidation mechanism has been shown to proceed through a similar general reaction scheme as that for alkanes [19,21]. H-atom abstraction, mainly by hydroxyl radicals, leads to the formation of methoxymethyl ($CH_3O\dot{C}H_2$) radicals. These can either undergo β-scission to form methyl radicals and formaldehyde or add to molecular oxygen to form alkyl-peroxyl ($CH_3OCH_2\dot{O}_2$) radicals. These can isomerize via a 6-membered transition state ring to form hydroperoxyl alkyl ($\dot{C}H_2OCH_2O_2H$) radicals. Similar to alkyl radicals, $\dot{C}H_2OCH_2O_2H$ radicals can either undergo β-scission, each forming two molecules of formaldehyde and a hydroxyl radical or add to molecular oxygen to form peroxy-hydroperoxyl-alkyl ($\dot{O}_2CH_2OCH_2O_2H$) radicals. At low temperatures, addition to O_2 dominates, and these radicals undergo a second isomerization reaction leading to the formation of stable HO_2CH_2OCHO molecules and reactive hydroxyl radicals. The subsequent decompositions of HO_2CH_2OCHO molecules yield more hydroxyl radicals and $\dot{O}CH_2OCHO$ radicals.

Table 5 presents a list of the low-temperature oxidation pathways of CH_3OCH_3. Here we have used Quantum-Rice–Ramsperger–Kassel (QRRK) theory with a modified strong-collision (MSC) model for energy transfer, to initially assess the pressure-dependencies of these low-temperature oxidation pathways.

The QRRK/MSC method herein [62] requires as input, a high-pressure limiting rate constant for each reaction pathway, Lennard-Jones parameters for the reactant and bath gas (N_2), and an estimate of the average energy transferred in deactivating collisions $\langle\Delta E_d\rangle$. As part of these calculations we employed the high-pressure limiting rate constants recommended by Li et al. [63] for the $CH_3O\dot{C}H_2$ radical β-scission, and the CBS-q calculations of Yamada et al. [58] for the remaining low-temperature oxidation reactions, Table 5.

For the energy transfer model, Miller and Klippenstein [64] performed RRKM/ME computations on *n*-propyl radical decomposition reactions and found that a temperature-dependent function, $\langle\Delta E_d\rangle = 110(T/300)^{1.0}\ cm^{-1}$, gave good agreement with experiment. We therefore adopt these energy transfer parameters for the structurally similar $CH_3O\dot{C}H_2$ radical. For the $R\dot{O}_2$ and $\dot{O}_2QOOH$ radical potential energy surfaces $\langle\Delta E_d\rangle = 200(T/300)^{0.85}\ cm^{-1}$ and $\langle\Delta E_d\rangle = 300(T/300)^{0.85}$ were estimated respectively, based on direct analogy to those used by Franklin Goldsmith et al. [65] for the corresponding radicals on the *n*-propyl + O_2 ($C_3H_7\dot{O}_2$) and $C_3H_7\dot{O}_2 + O_2$ potential energy surfaces.

The Lennard-Jones parameters for the $CH_3O\dot{C}H_2$ radical were determined empirically from the correlations of Kee et al. [66], where the critical constants of DME [67] were employed to calculate $\sigma = 4.71$ Åand $\varepsilon/k_B = 296.6$ K. For the $R\dot{O}_2$ and $\dot{O}_2QOOH$ radicals, the Lennard-Jones parameters used by Goldsmith et al. [65] were adopted. All computations were carried out in an N_2 bath gas with Lennard-Jones parameters of $\sigma = 3.681$ Å$\varepsilon/k_B = 67.89$ K used as in the study of Jasper and Miller [68].

Table 5
Low-temperature DME reactions treated as pressure dependent.

$CH_3O\dot{C}H_2 \rightleftarrows \dot{C}H_3 + CH_2O$
$CH_3O\dot{C}H_2 + O_2 \rightleftarrows CH_3OCH_2\dot{O}_2$
$CH_3O\dot{C}H_2O_2 \rightleftharpoons \dot{C}H_2OCH_2O_2H$
$\dot{C}H_2OCH_2O_2H \rightarrow CH_2O + CH_2O + \dot{O}H$
$\dot{C}H_2OCH_2O_2H + O_2 \rightleftarrows \dot{O}_2CH_2OCH_2O_2H$
$\dot{O}_2CH_2OCH_2O_2H \rightleftharpoons HO_2CH_2OCHO + \dot{O}H$

The initial QRRK/MSC computations were incorporated into the kinetic mechanism, and it was found that the pressure-dependency of the $CH_3O\dot{C}H_2$ radical decomposition were particularly sensitive in predicting ignition delay times. We have therefore re-evaluated $k(T,p)$ for this reaction *via* quantum chemistry and TST/RRKM/ME computations. Geometry optimisation, frequency and single-point energy calculations were carried out using the CBS-QB3 [69], CBS-APNO [70] and G3 [71] compound methods. Relaxed potential energy surface scans of dihedral angles were carried out in 10 ° increments using the B3LYP method [72,73] with a CBSB7 basis set, and the computed rotational barriers were used in 1-D hindered internal rotation treatments. Gaussian 09 [74] has been used for quantum chemical calculations with the ChemRate [75] code used for the statistical rate theory calculations. An energy grain size of 30 cm^{-1} was used for the computation of densities and sums of states of the reactant and transition state, and thus microscopic rate constants, up to a maximum energy of 100,000 cm^{-1}, with a time-dependent solution of the master equation ultimately employed.

A high-pressure limiting rate constant of $8.03 \times 10^{12}\ T^{0.44}\ \exp(13,330/T)\ s^{-1}$ follows based on B3LYP/CBSB7 ro-vibrational properties and a CBS-QB3 barrier of 106.9 kJ mol^{-1} (0 K). The high-pressure limiting rate constant is within 14–64% of that proposed by Li et al. [63] from 500 to 2000 K, and the results of *this study* therefore corroborate their recommendation.

Figure 3 presents the pressure-dependent rate constants used in *this study* and compares them to the available literature rate constants for β-scission of the $CH_3O\dot{C}H_2$ radical. At 1000 K and 10 atm, our computed rate constant is a factor of 8.6 slower than the high-pressure limiting one. The rate constants used for this reaction in the two studies of Curran/Fischer et al. [19,20] and Zhao et al. [21] are approximately a factor of 2.3 and 3.5 slower than the high-pressure limiting rate constant calculated by Li et al. [63] at this temperature respectively, and a factor of 6.3 and 9.7 lower than the high-pressure limiting rate constant recommended in *this study*. The study of Zhao et al. [21] found that using the rate constant of Li et al. [63] meant that they could not achieve accurate predictions in particular for intermediate temperatures (800–1000 K), for both flow reactor data and ignition delay times. It is interesting to note that the estimations of Curran/Fischer et al. [19,20] and Zhao et al. [21] are in close agreement with the pressure-dependent rate constants used at 10 atm in this study, possibly indicating why they had to alter the high-pressure limiting rate constant recommended by Li to achieve agreement with experiment.

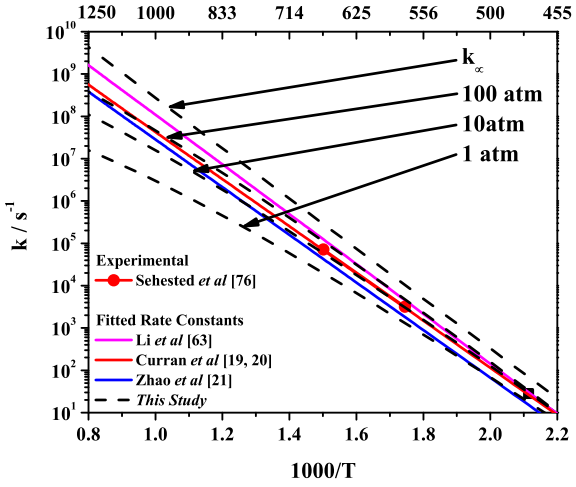

Fig. 3. Rate constants for $CH_3O\dot{C}H_2 \rightleftharpoons \dot{C}H_3 + CH_2O$.

Figure 4 shows the difference observed when pressure-dependent rate constants were included in the mechanism. It also shows that the change in the predictions is mainly due to the pressure-dependent treatment of $CH_3O\dot{C}H_2 \rightleftarrows \dot{C}H_3 + CH_2O$. Figure 4 also illustrates the improvement in the predictions compared to the previous model of Curran/Fischer et al. [19,20]. Ultimately, it is the pressure-dependent treatment of the methoxymethyl radical β-scission that has the greatest effect on model predictions. The pressure-dependent treatment of the other reactions listed in Table 5 has a minor effect on the model predictions when compared to the effect of the methoxymethyl radical β-scission. The QRRK/MSC approach used to assess the pressure-dependency of these reactions is therefore not updated to a more sophisticated RRKM/ME treatment, as the added expense of the latter is unlikely to offer any great improvements with respect to the final model predictions.

Finally, the rate constant for the decomposition of the carbonyl-hydroperoxide species $HO_2CH_2OCHO \rightleftarrows \dot{O}CH_2OCHO + \dot{O}H$ was adapted from the study of Sahetchian et al. [76]. This rate constant was increased by a factor of 5 to gain agreement with our low-temperature RCM data. The previous studies of Curran/Fischer et al. [19,20] and Zhao et al. [21] required unreasonable increases in this rate constant of factors of approximately 10 and 24, respectively, to achieve model agreement with experiment.

5. Results and discussion

As mentioned above, the shock-tube results for 80/20 and 60/40 CH_4/DME mixtures have been described in the thesis of Zinner

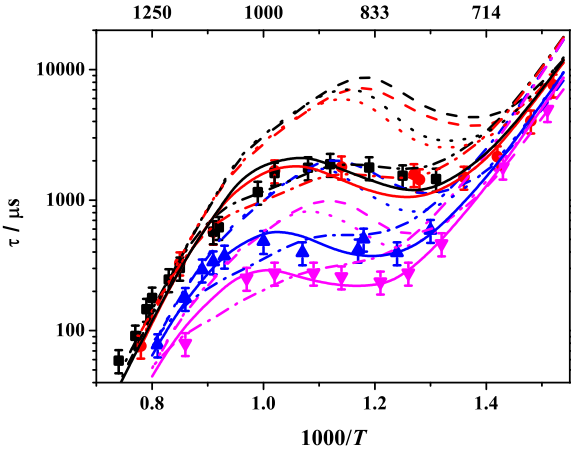

Fig. 4. Comparison of ignition delay times over a range of pressures for DME in 'air' ϕ = 1.0 from this study (p_5 = 11.9 and 25.0 atm) and Pfahl et al. [35] (p_5 = 12.8 and 39.5 atm). Symbols are experimental results; ■ – p_5 = 11.9 atm, ● – p_5 = 12.8 atm, ▲ – p_5 = 25.0 atm, ▼ – p_5 = 39.5 atm. Solid lines are predictions using the current mechanism using pressure-dependent rate constants, dashed lines represent the predictions of the current mechanism using high-pressure limiting rate constants, dotted lines represent the predictions using pressure-dependent rate constants for all reactions except methoxymethyl radical β-scission and dash-dot lines represent the predictions of the Curran/Fischer et al. mechanism [19,20].

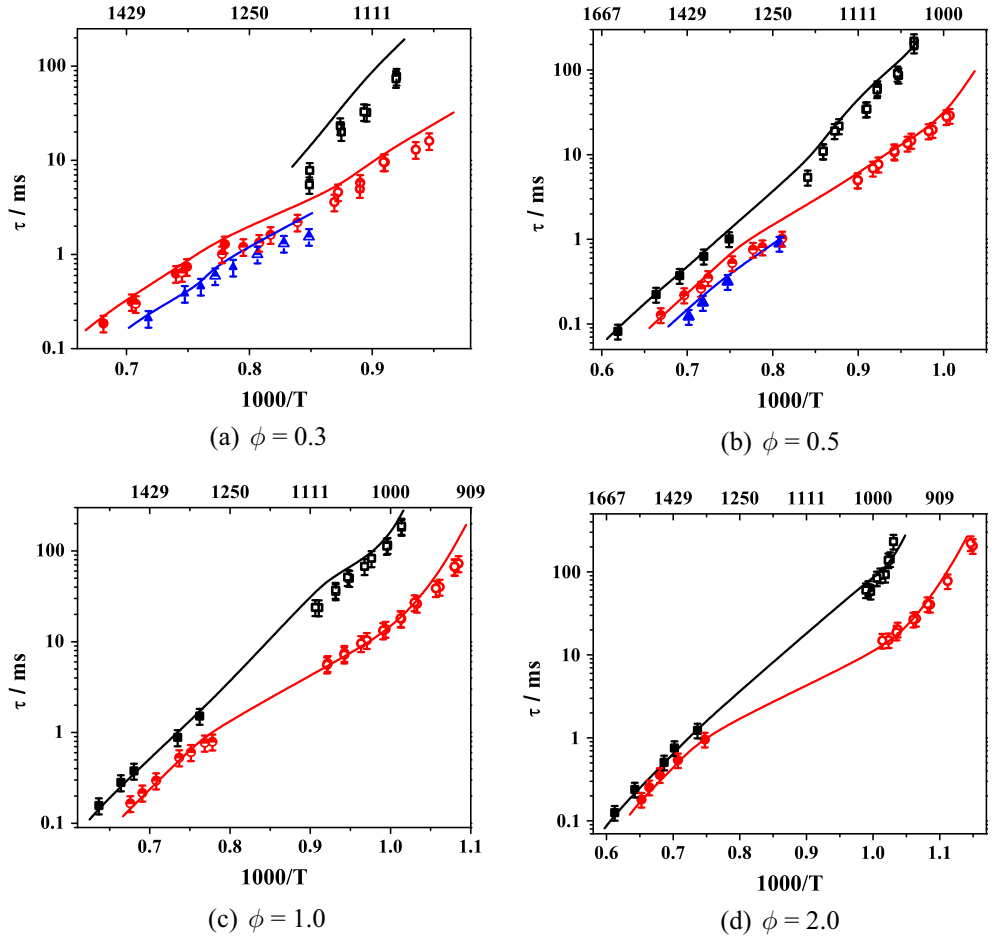

Fig. 5. Influence of pressure on pure methane in air mixtures at ■ – ~ 10 atm, ● – 25 atm (15 atm for Fig. 5(d) ST data), ▲ – 44 atm. Open symbols are RCM data, filled symbols ST data, half-filled symbols are tailored-interface ST data. Lines are Mech_56.54 predictions.

[49], and the shock-tube results for both of the pure fuels were presented in a conference paper [50], but neither set has been published formally in an archival journal until now. The tailored shock-tube data (presented as half-filled symbols) and the RCM data are presented for the first time in the present study. This section first presents the pure CH_4 data and the chemistry which describes its oxidation under the conditions studied here. This first section is followed by the extensive set of experimental results and model analyses for 80/20 CH_4/DME blends. The results for the 60/40 blends are similar from a chemistry point of view and are included as Supplementary Material. Pure DME mixtures are then presented and discussed. Finally, the relative reactivities of the pure fuels and their mixtures are compared and discussed.

5.1. Methane oxidation

Methane data are presented as a function of pressure in Fig. 5. It is observed that ignition delay times decrease with increasing temperature and pressure, as expected. Mech_56.54 captures the overall trends in the experimental data quite well but tends to under-predict reactivity at 10 atm and at the lower-temperature conditions of the RCM experiments.

An intermediate temperature of 1177 K was chosen to perform brute-force sensitivity analyses as a function of pressure for data in Fig. 5(a). Figure 6 shows that for all pressures the most promoting reaction is $\dot{C}H_3 + O_2 \rightleftarrows CH_2O + \dot{O}H$. While the most inhibiting reaction under all conditions is methyl radical recombination to form ethane. From 9.9 atm to 41.6 atm, the sensitive reactions do not change; this is an indication that it is not a change in the controlling chemistry that causes the observed decrease in ignition delay time with increasing pressure but the increased concentration of reactants (CH_4 and O_2).

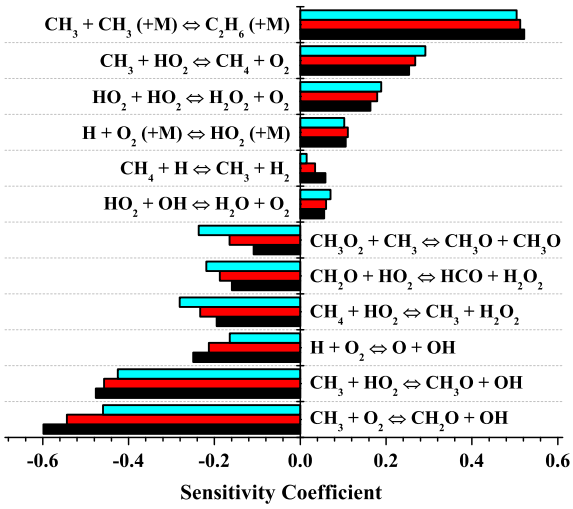

Fig. 6. Sensitivity analyses at 1177 K and at $\phi = 0.30$, ■ – 9.9 atm, ■ – 19.7 atm, ■ – 41.6 atm.

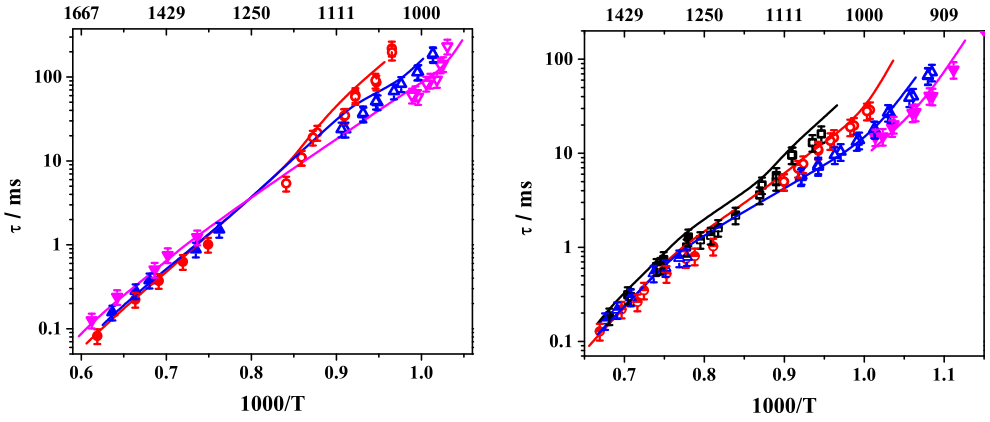

(a) 10 atm (b) 25 atm

Fig. 7. Influence of equivalence ratio on CH_4 mixtures at ■ – $\phi = 0.3$, ● – $\phi = 0.5$, ▲ – $\phi = 1.0$, ▼ – $\phi = 2.0$. Open symbols are RCM data, filled symbols ST data, half-filled symbols are tailored-interface ST data. Lines are Mech_56.54 predictions.

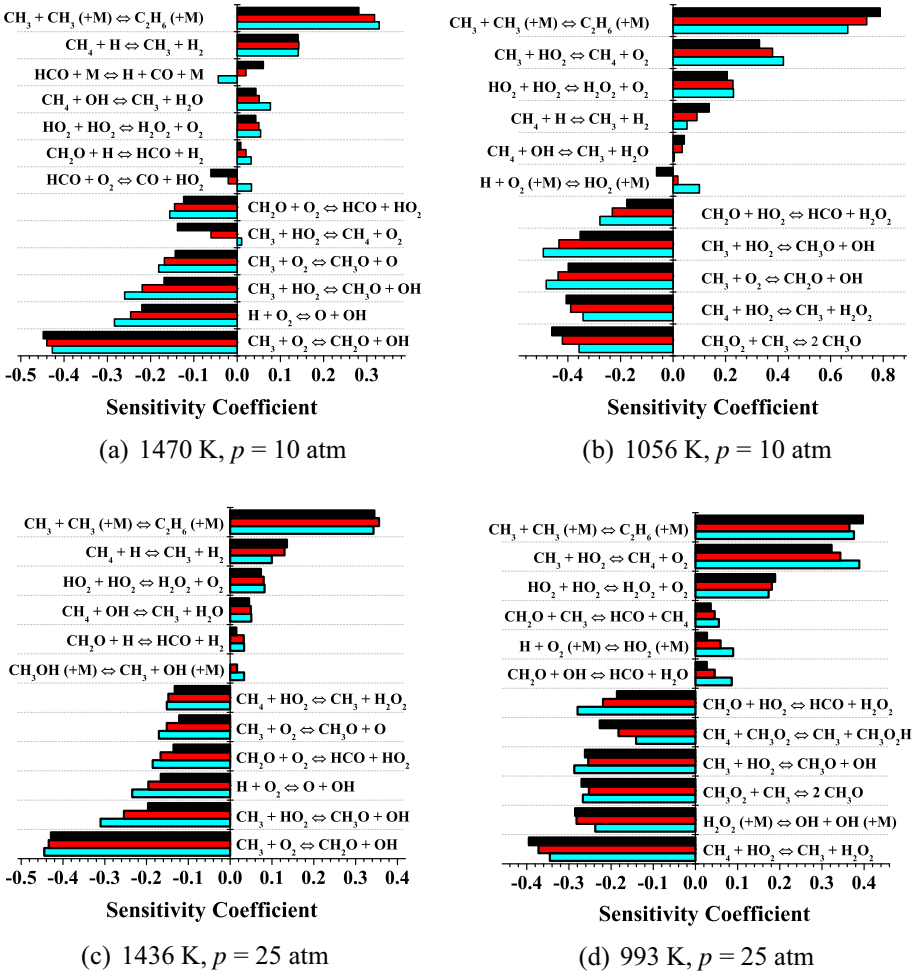

(a) 1470 K, $p = 10$ atm (b) 1056 K, $p = 10$ atm

(c) 1436 K, $p = 25$ atm (d) 993 K, $p = 25$ atm

Fig. 8. Sensitivity analyses CH_4/'air' mixtures, ■ – $\phi = 2.0$, ■ – $\phi = 1.0$, ■ – $\phi = 0.5$.

Figure 7 presents ignition delay times for pure methane mixtures at equivalence ratios of $\phi = 0.3$–2.0 and pressures of 10 and 25 atm. Figure 7(a) shows that, at the lowest temperatures, ignition delay times decrease with increasing equivalence ratio. However the opposite trend is true for experimental data above 1312 K. This inversion in the effect of equivalence ratio is not seen in Fig. 7(b) where ignition times decrease with increasing equivalence ratio. There is an overlap of ignition delay times of varying equivalence ratios at the highest reflected-shock temperatures presented; this is most evident at temperatures above 1430 K.

Figure 8 depicts brute-force sensitivity analyses performed for the experimental conditions presented in Fig. 7. Figure 8(a) and

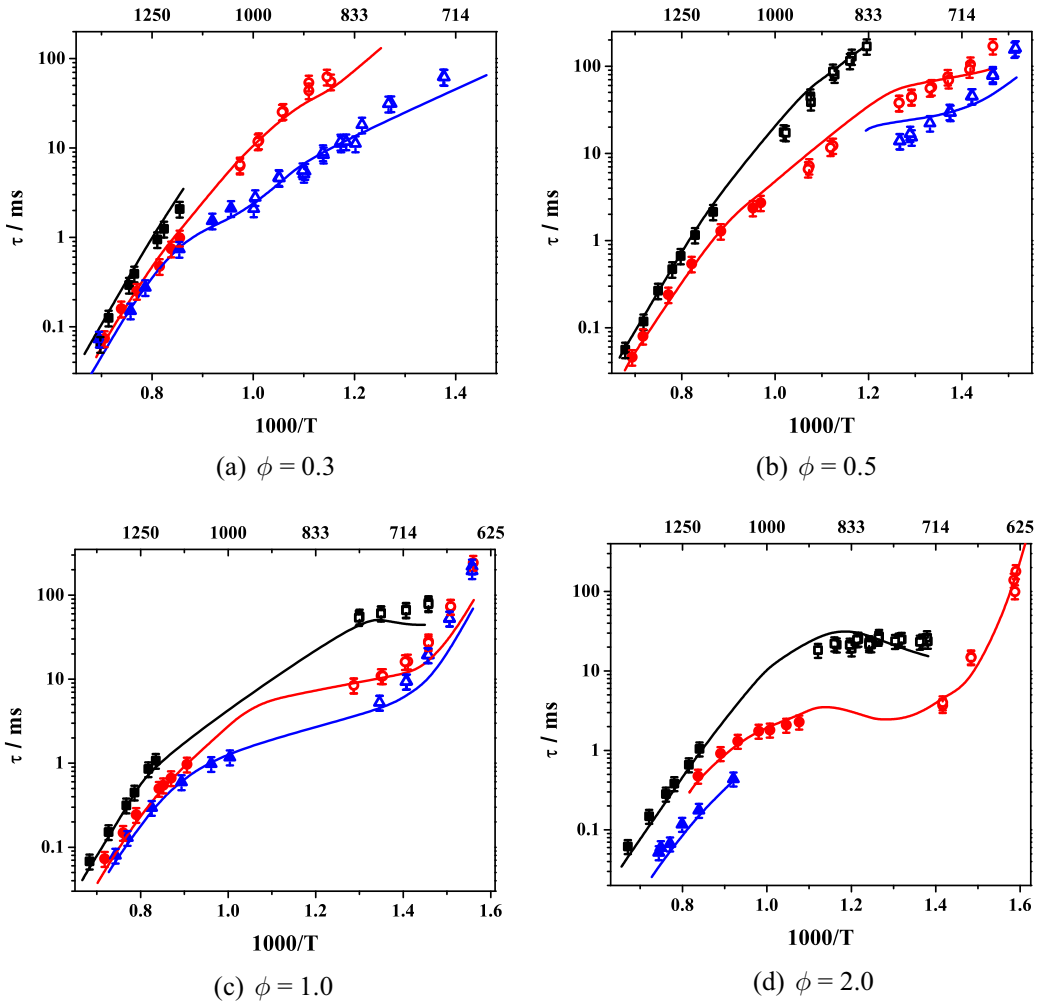

Fig. 9. Influence of pressure on 80/20 CH_4/DME mixtures. ■ – ~ 10 atm, ● – ~ 20 atm, ▲ – ~ 30 atm. Open symbols are RCM data, filled symbols ST data. Lines are Mech_56.54 predictions.

(b) present high and low temperature (1470 and 1056 K) sensitivity analyses at $p = 10$ atm. Figure 8(c) and (d) present high and low temperature (1436 and 993 K) sensitivity analyses at $p = 25$ atm. Under all of the conditions shown the most inhibiting reaction is methyl radical recombination to form ethane. For both pressures the reaction $CH_3\dot{O}_2 + \dot{C}H_3 \rightleftarrows CH_3\dot{O} + CH_3\dot{O}$, promotes reactivity at low-temperature. Both reactants are fuel derived and as a result, fuel-rich mixtures have faster ignition delay times at low temperatures. At high temperature for both pressures ($p = 10$ atm and 25 atm), the reaction $\dot{H} + O_2 \rightleftarrows \ddot{O} + \dot{O}H$ becomes the most promoting one leading to the inversion in the effect of equivalence ratio at $p = 10$ atm. This inversion is observed at $p = 10$ atm but is not seen at $p = 25$ atm, and at the highest temperatures studied in Fig. 7(b) there is no effect of equivalence ratio. This overlap of equivalence ratios was noted at $T = 1250$ K for the 10 atm data. The inversion temperature for the 25 atm data is increased at higher pressure as the rate constant for the reaction $\dot{C}H_3 + O_2(+M) \rightleftarrows CH_3\dot{O}_2(+M)$ is pressure-dependent and increases with pressure. Therefore, at higher pressure the equilibrium of this reaction favors the formation of $CH_3\dot{O}_2$ radicals up to higher temperatures when compared to the 10 atm data.

5.2. 80% CH_4/20% DME

Ignition delay times were measured for mixtures of 80/20 CH_4/DME. The results of the experimental data and computational simulations are presented in Fig. 9 as a function of pressure. Similar to pure methane, the 80/20 CH_4/DME blend shows that ignition delay times globally decrease with increasing pressure.

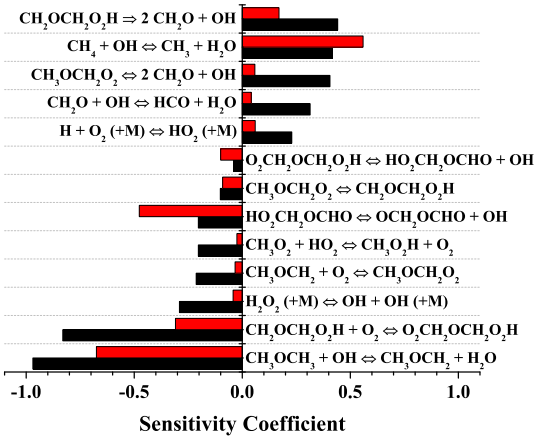

Fig. 10. Sensitivity to ignition delay time at 706 K, $\phi = 2.0$ at ■ – 5.9 atm, ■ – 25.3 atm.

Figure 10 presents brute-force sensitivity analyses adhering to the conditions presented in Fig. 9(d) $\phi = 2.0$ in 'air' mixtures at 706 K. What is notable is that under the conditions studied, the

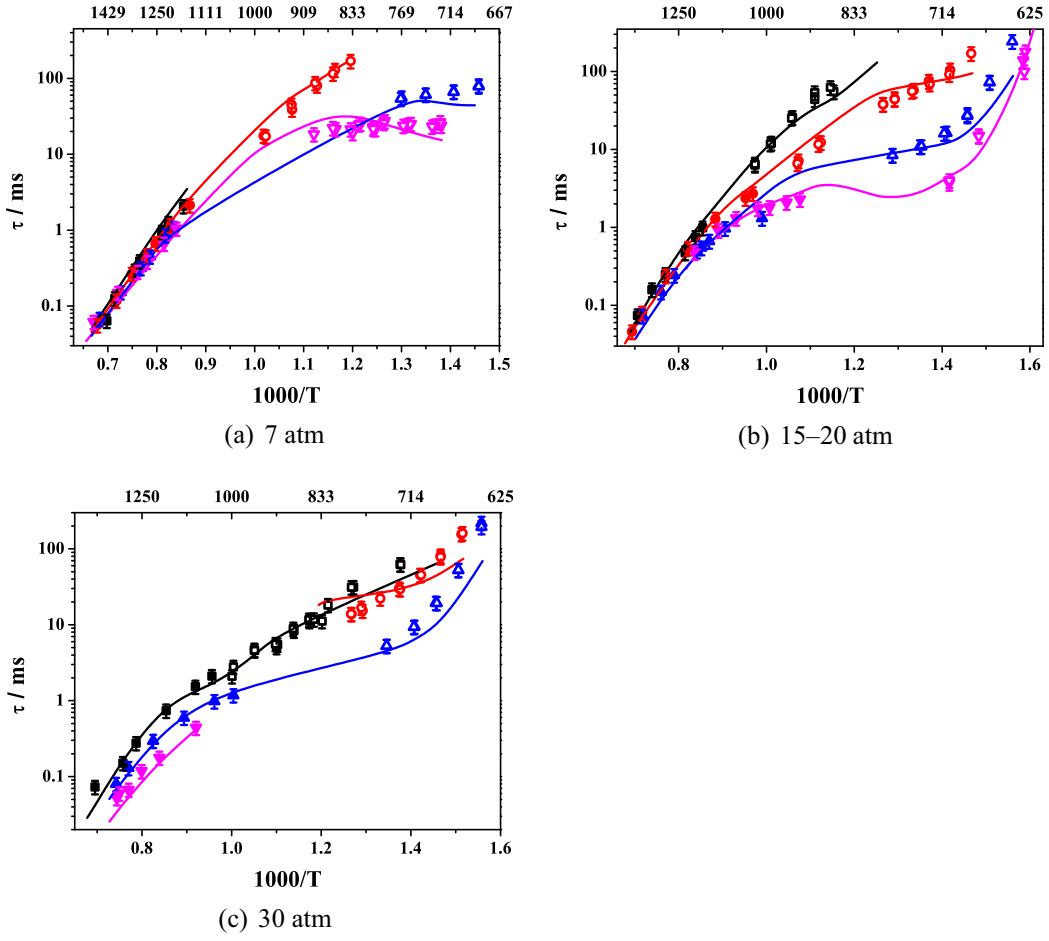

Fig. 11. Influence of equivalence ratio for 80/20 CH_4/DME mixtures. ■ – ϕ = 0.3, ● – ϕ = 0.5, ▲ – ϕ = 1.0, ▼ – ϕ = 2.0. Open symbols are RCM data, filled symbols ST data. Lines are Mech_56.54 predictions.

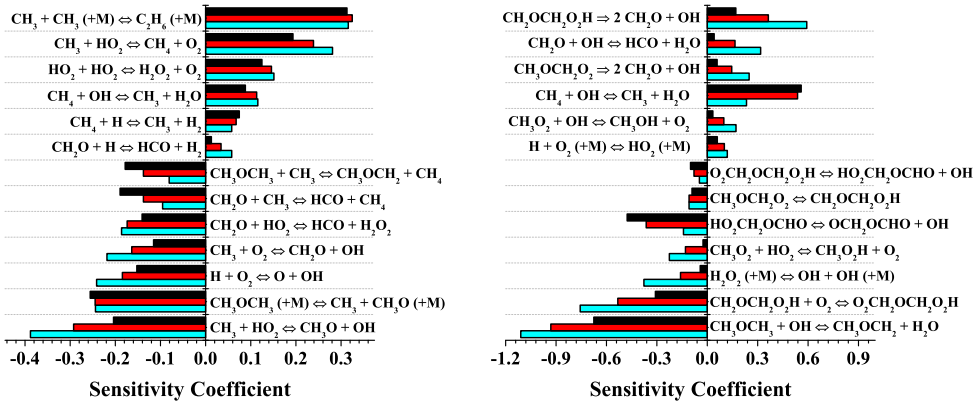

Fig. 12. Sensitivity analyses for ignition delay times at p = 10 atm and at ■ – ϕ = 2.0, ■ – ϕ = 1.0, ■ – ϕ = 0.5.

most-sensitive reactions are those involving DME. For example, the most-promoting reaction is $CH_3OCH_3 + \dot{O}H \rightleftarrows CH_3O\dot{C}H_2 + H_2O$, while the most-inhibiting reaction is $\dot{C}H_2OCH_2O_2H \rightarrow CH_2O + CH_2O + \dot{O}H$. This high sensitivity to DME is interesting because, despite the fact that there is four times more methane present in the blend, the reactions controlling ignition involve DME chemistry. Pure methane is unreactive at 706 K, but with the addition of a small quantity of DME its reactivity increases significantly. At approximately 1150 K and 10 atm, ignition delay time decreases by a factor of 5.1 from pure methane to 80/20 CH_4/DME. From the point of view of gas turbine operation at low temperatures, this decrease in the ignition delay time as a function of DME addition is significant as the addition of only small quantities of DME could theoretically be used to tailor the operation of the gas turbine for a given temperature and pressure.

Figure 11 presents ignition delay times and model simulations for the 80/20 CH_4/DME blends as a function of equivalence ratio. Figure 11(b) shows that ignition delay times decrease with

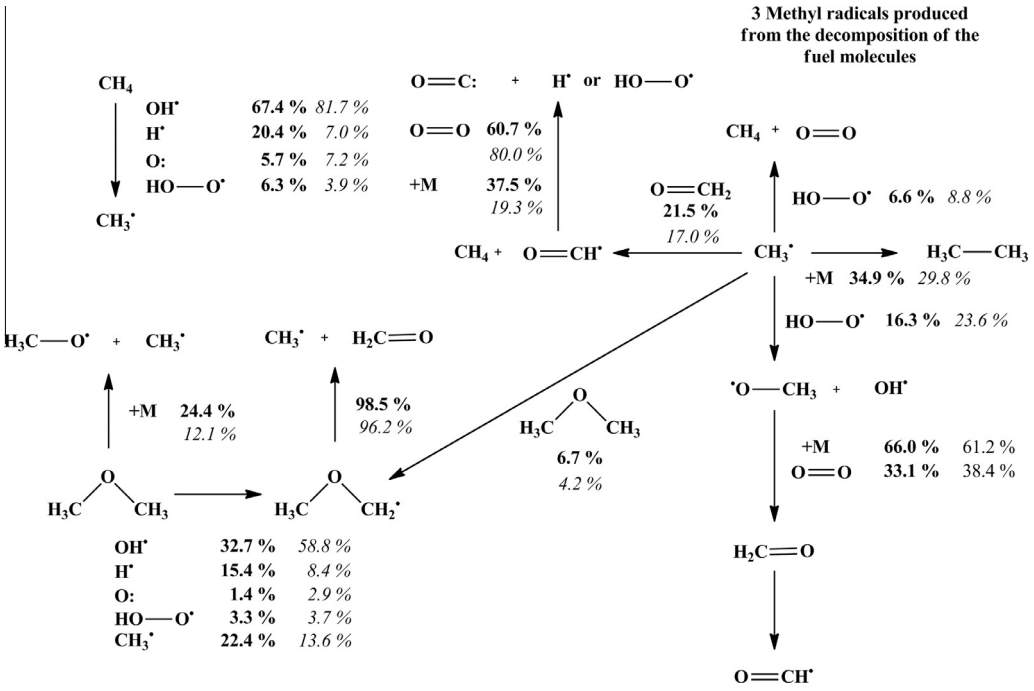

Fig. 13. Flux analyses at 1250 K and p = 17.0 atm in 'air', ϕ = 2.0 – bold font, ϕ = 0.5 – italic font.

increasing equivalence ratio at low temperatures (<1100 K). Figure 11(a) shows that ignition delay time is independent of equivalence ratio in the temperature range 1200–1490 K. Mech_56.54 predicts all of these trends very well.

Figure 12 presents the results of sensitivity analyses on mixtures shown in Fig. 11(b) at 1250 K and 706 K. These temperatures were chosen to show the change in the sensitive reactions from low to high temperature. As discussed above, the 80/20 blend reactivity at low temperature is controlled primarily by DME-containing reactions. All equivalence ratios show sensitivity to DME reactions, Fig. 12(b). The three most-promoting reactions for all three equivalence ratios are listed below.

$$CH_3OCH_3 + \dot{O}H \rightleftarrows CH_3O\dot{C}H_2 + H_2O$$

$$\dot{C}H_2OCH_2O_2H + O_2 \rightleftarrows \dot{O}_2CH_2OCH_2O_2H$$

$$HO_2CH_2OCHO \rightleftarrows \dot{O}CH_2OCHO + \dot{O}H$$

Figure 14(a) shows sensitivity analyses at 1250 K. The most-promoting reactions are $\dot{C}H_3 + H\dot{O}_2 \rightleftarrows CH_3\dot{O} + \dot{O}H$ and $CH_3OCH_3(+M) \rightleftarrows CH_3\dot{O} + \dot{C}H_3(+M)$. The most-inhibiting reactions are $\dot{C}H_3 + H\dot{O}_2 \rightleftarrows CH_4 + O_2$ and $\dot{C}H_3 + \dot{C}H_3(+M) \rightleftarrows C_2H_6(+M)$.

Figure 13 shows the results of flux analyses for data shown in Fig. 11(b) at 1250 K. Similar to the sensitivity analyses, the flux analyses show that methyl radical chemistry is very important. Methyl radicals are produced by H-atom abstraction reactions from CH_4 and unimolecular decomposition of DME. β-Scission of the methoxymethyl radical also produces methyl radicals. Unimolecular decomposition of DME is the second most-sensitive reaction over all equivalence ratios; this shows that DME is controlling ignition at high temperature as well as low temperatures.

The same trends in experimental data are observed for the 60/40 CH_4/DME blends. The controlling chemistry is the same as that described for the 80/20 CH_4/DME blends. These similar results are not surprising since DME chemistry is controlling ignition for the 80/20 blends, so it logically follows that it is also controlling ignition for the 60/40 blends which contain even more DME. All the results and analyses for the 60/40 mixtures are included as Supplementary Material.

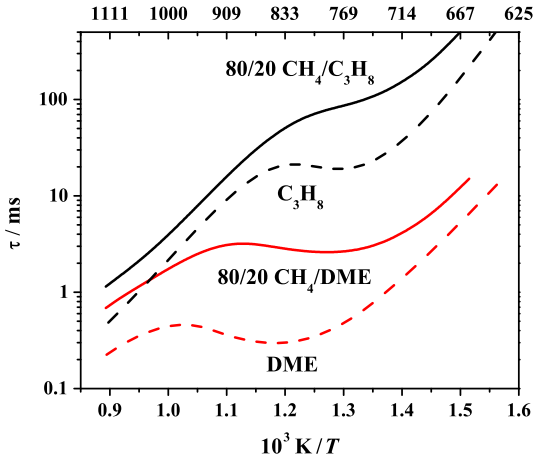

Fig. 14. Model predictions for n-C_3H_8, DME, and 80/20 CH_4/(DME or n-C_3H_8) in 'air' mixtures at p = 30 atm. Black lines are n-C_3H_8, red lines are DME. Solid line are 80/20 mixtures, dashed lines are pure fuels. (For interpretation of the references to colour in this figure legend, the reader is referred to the web version of this article.)

CH_4/DME is iso-electronic when compared to CH_4/C_3H_8, this provides an interesting comparison. Figure 14 shows that reactivity is increased overall in CH_4/DME blends when compared to CH_4/C_3H_8. The C–H bonds in DME are weaker than the C–H bonds in propane. This is due to the oxygen atom present in DME. This increases the overall reactivity of DME when compared to propane. Propane has an extra chain propagation $H\dot{O}_2$ elimination pathway, $C_3H_7\dot{O}_2 \rightleftarrows C_3H_6 + H\dot{O}_2$, that is not possible in the DME oxidation mechanism. Thus, there are more chain propagation pathways possible for propane compared to DME which only has the β-scission of the hydroperoxy-alkyl radical to two molecules of formaldehyde and $\dot{O}H$ radical. This also contributes to the reduced reactivity.

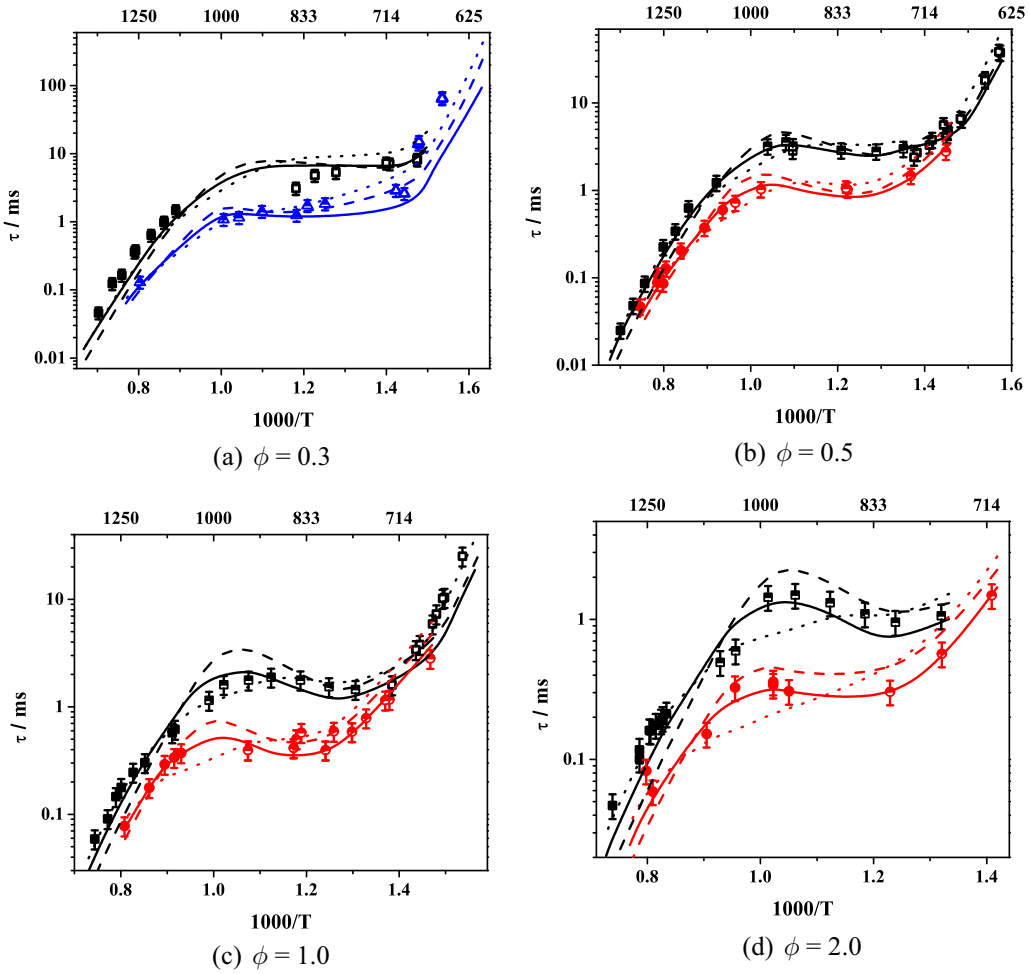

Fig. 15. Influence of pressure on DME mixtures, ■ – ~11 atm, ● – ~25 atm, ▲ – ~30 atm. Open symbols are RCM data, filled symbols ST data, half filled symbols are tailored interface data. Solid lines – Mech_56.54, dashed lines – Zhao et al. [21], dotted lines – Curran et al. [19,20].

5.3. Dimethyl ether oxidation

Ignition delay times for pure DME in 'air' mixtures are presented in Fig. 15 comparing the effect of pressure over four equivalence ratios. DME displays a negative temperature coefficient (NTC) region where the ignition delay times increase with increasing temperature. The temperature at which NTC behavior begins is dependent on both the mixture composition and on the pressure studied. As equivalence ratio increases, so does the temperature at which the NTC behavior begins. The same effect is noted as the pressure increases. Overall, ignition delay times decrease as the pressure increases. As in Sections 5.1 and 5.2, this decrease is mainly due to the increase in the concentration of reactants with pressure.

Mech_56.54 predictions together with those by the Zhao et al. [21] and Curran et al. [19,20] mechanisms are compared to the experimental data. Mech_56.54's predictions offer an improvement over previous mechanisms for all conditions shown. Improvements in predictions are seen at high temperatures (>1000 K) when compared to the Zhao et al. [21] mechanism, and at low temperatures (<800 K) when compared to the mechanism of Curran et al. [19,20].

Brute-force sensitivity analyses were carried out under the conditions shown in Fig. 15(b) at $\phi = 0.5$ in 'air' and 827 K. This temperature was chosen as it showed the largest effect of pressure on ignition delay times. Similar to pure methane and the 80/20 blends, the most-sensitive reactions are the same for the two pressures Fig. 16. This common result reinforces the idea that the decrease in ignition delay time is largely due to increased concentrations at higher pressure, rather than a difference in the reactions controlling ignition. The most-inhibiting reaction for both pressures is $\dot{C}H_2OCH_2O_2H \rightarrow CH_2O + CH_2O + \dot{O}H$, while the most-promoting reaction for both pressures is $\dot{C}H_2OCH_2O_2H + O_2 \rightleftarrows \dot{O}_2CH_2OCH_2O_2H$.

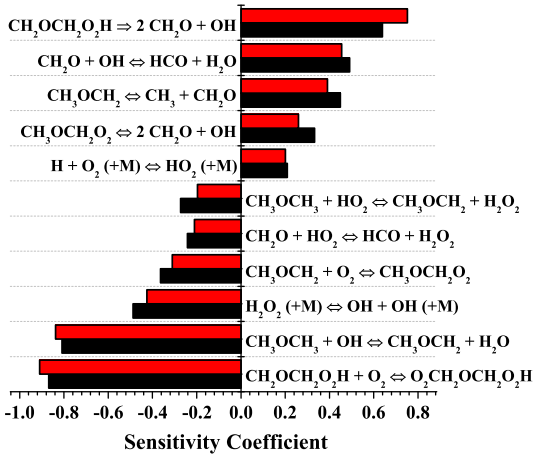

Fig. 16. Sensitivity analysis at 827 K and $\phi = 0.50$ at ■ – 12.4 atm, ■ – 24.7 atm.

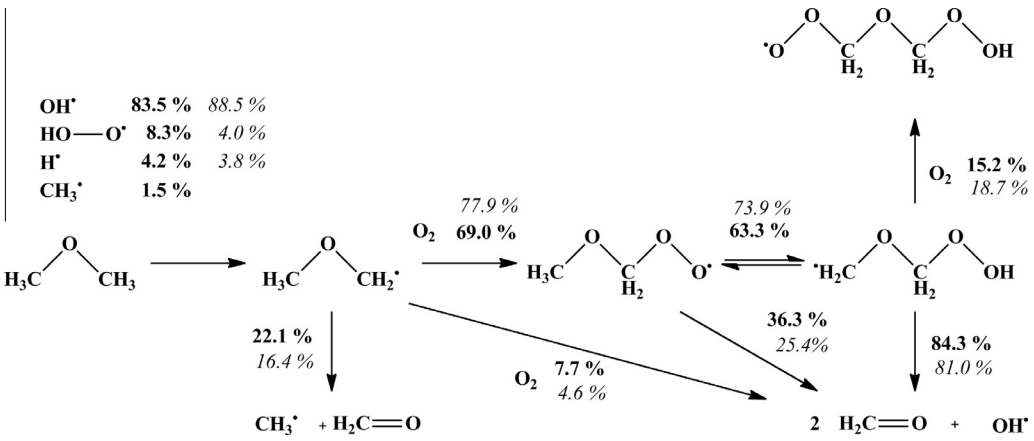

Fig. 17. Flux analyses at 827 K and $\phi = 0.50$, 12.4 atm – bold font, 24.7 atm – italic font.

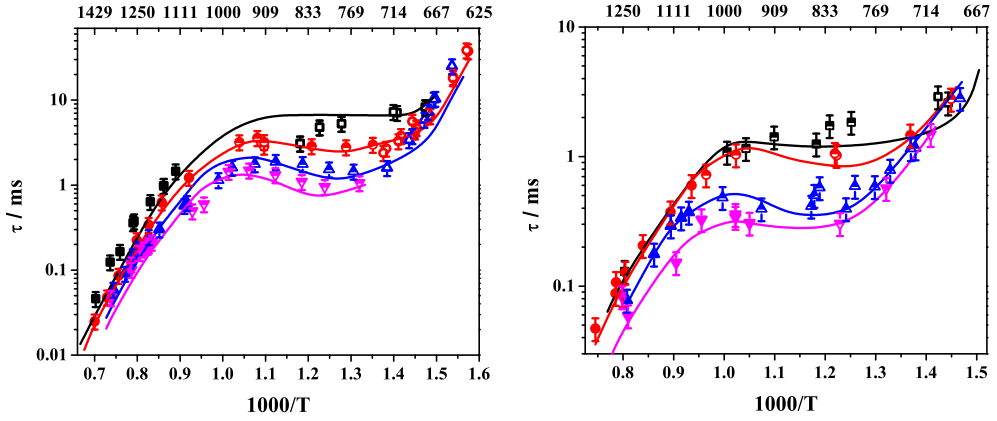

(a) 11 atm (b) 25–30 atm

Fig. 18. Influence of equivalence ratio for DME mixtures. ■ – $\phi = 0.3$, ● – $\phi = 0.5$, ▲ – $\phi = 1.0$, ▼ – $\phi = 2.0$. Open symbols are RCM data, filled symbols ST data, half-filled symbols are tailored-interface ST data. Lines are Mech_56.54 predictions.

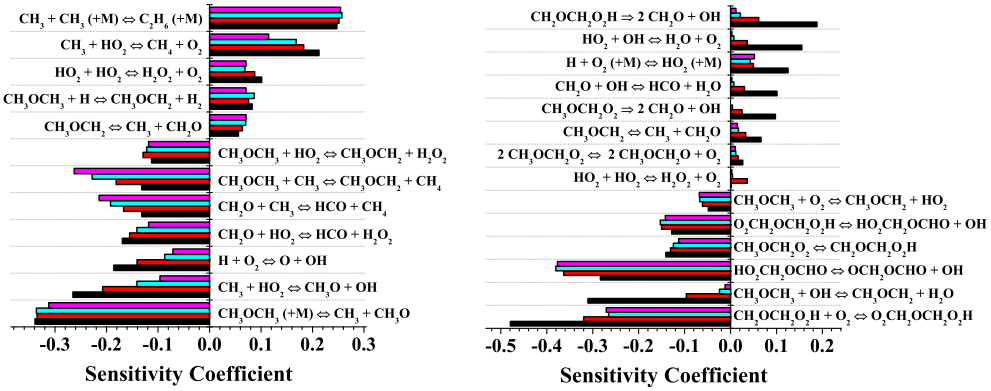

(a) 1250 K (b) 670 K

Fig. 19. Sensitivity analyses at $p = 10$ atm and at ■ – $\phi = 0.3$, ■ – $\phi = 0.5$, ■ – $\phi = 1.0$, ■ – $\phi = 2.0$.

Figure 17 shows flux analyses at a temperature of 827 K for the two pressures presented in the sensitivity analyses. Both pressures show that DME is consumed by H-atom abstraction forming methoxymethyl radical. Methoxymethyl radical is consumed through three reactions:

(1) $CH_3O\dot{C}H_2 \rightleftarrows \dot{C}H_3 + CH_2O$.
(2) $CH_3O\dot{C}H_2 + O_2 \rightarrow CH_2O + CH_2O + \dot{O}H$.
(3) $CH_3O\dot{C}H_2 + O_2 \rightleftarrows CH_3OCH_2\dot{O}_2$.

At both pressures of 12.4 and 24.7 atm, the dominant reaction is R3. At 24.6 atm 11.1%, more of the methoxymethyl radical is

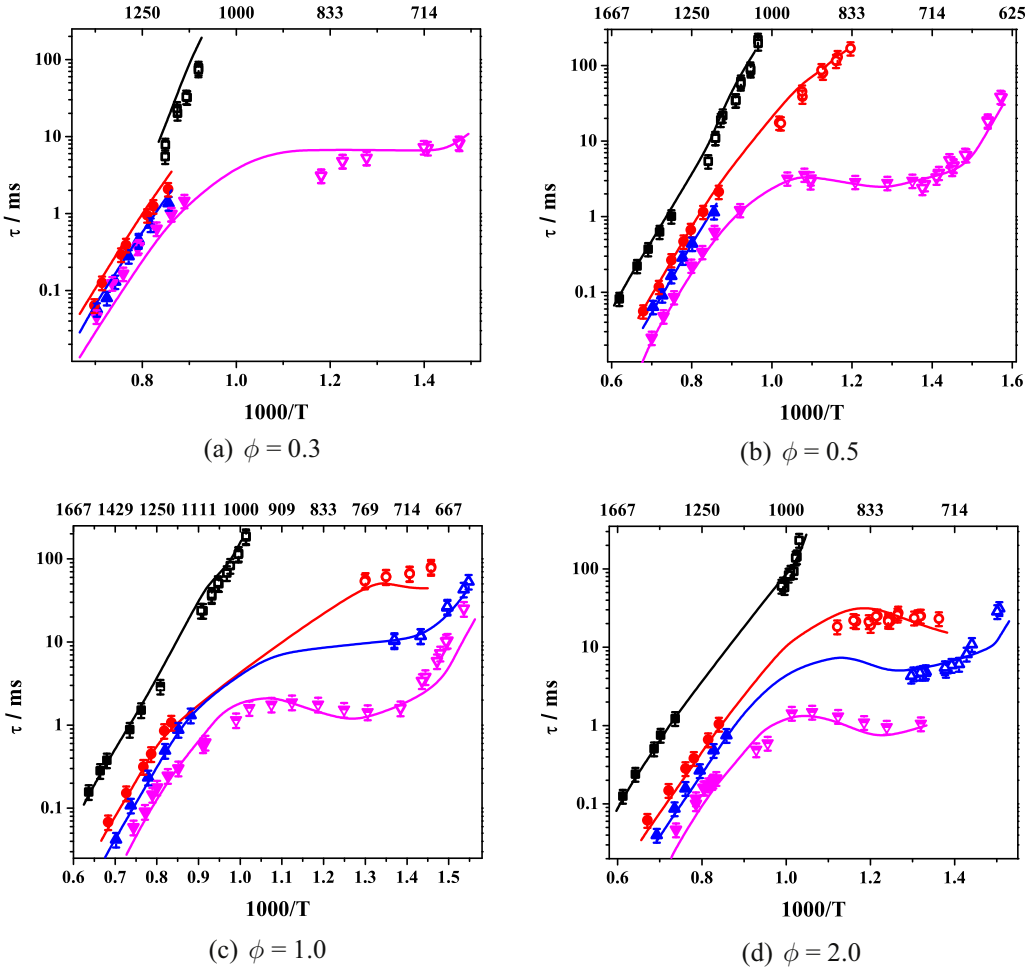

Fig. 20. Influence of mixture composition at p = 7–10 atm, ■ – CH_4, ● – 80/20 CH_4/DME, ▲ – 60/40 CH_4/DME, ▼ – DME. Open symbols are RCM data, filled symbols ST data, half-filled symbols are tailored-interface ST data. Lines are Mech_56.54 predictions.

consumed via R3 compared to 12.4 atm. The methoxymethyl radical can react via the chemically activated reaction (R2) so that at lower pressure, chemically activated $CH_3OCH_2\dot{O}_2$ radicals are formed and decompose directly to products. Figure 17 supports this idea because at 12.4 atm, 2.4% more of the methoxymethyl radical is consumed by R2 when compared to 24.6 atm. A similar trend is observed for the consumption of $CH_3OCH_2\dot{O}_2$ radicals. In previous models [19–21] these chemically activated reactions were not considered.

The sensitivity analyses indicates that the fate of the $\dot{C}H_2OCH_2O_2H$ radical is all important as it is associated with the two most sensitive reactions, R4 and R5:

(4) $\dot{C}H_2OCH_2O_2H \rightarrow CH_2O + CH_2O + \dot{O}H$.
(5) $\dot{C}H_2OCH_2O_2H + O_2 \rightleftarrows \dot{O}_2CH_2OCH_2O_2H$.

R4 is the most-inhibiting reaction, while R5 is the most-promoting reaction. R4 inhibits reactivity as it produces two stable formaldehyde molecules and one hydroxyl radical, whereas R5 leads to the formation of $\dot{O}_2CH_2OCH_2O_2H$ radicals, which ultimately lead to chain branching.

Figure 17 shows that, under the conditions analyzed, the $\dot{C}H_2OCH_2O_2H$ radical is consumed predominantly via R4. The formaldehyde produced competes with DME for hydroxyl radicals, and this leads to decreased reactivity. In Fig. 18, ignition delay times for pure DME are compared as a function of equivalence ratio (ϕ = 0.3–2.0 in 'air') for two pressures. Ignition delay times decrease with increasing equivalence ratio over all temperatures and pressures presented. As equivalence ratio increases, so too does the temperature at which NTC behavior begins.

Sensitivity analyses were performed at low temperatures (670 K), Fig. 19(a), and high (1250 K) temperatures, Fig. 19(b), for mixtures corresponding to Fig. 18(a). In contrast to the analyses for pure methane oxidation, the reactions controlling DME ignition at the two temperatures are very different. For example, sensitivity analyses for pure methane showed that at both low and high temperatures, methyl radical recombination was the most inhibiting reaction. In contrast, DME shows methyl radical recombination is only sensitive at high temperatures. At low temperatures, the most-inhibiting reaction is $\dot{C}H_2OCH_2O_2H \rightarrow CH_2O + CH_2O + \dot{O}H$ as it competes with the $\dot{C}H_2OCH_2O_2H$ radical addition to molecular oxygen, which subsequently proceeds to chain branching. This reaction is seen to be highly promoting for all four equivalence ratios at low temperatures (600–900 K). It is the most-promoting reaction for ϕ = 0.3 in 'air' and the second most-promoting reaction for the other three equivalence ratios. The most-promoting reaction at ϕ = 0.5, 1.0 and 2.0 in 'air' is $HO_2CH_2OCHO \rightleftarrows \dot{O}CH_2OCHO + \dot{O}H$. This reaction produces two radical species from one stable molecule, and thus it has a promoting effect on ignition. An interesting note is that all the reactions associated with DME low-temperature chemistry (listed in Table 5) are highlighted as being important in the low-temperature sensitivity analyses (see Fig. 19).

The most-inhibiting reaction for pure DME at high temperatures is methyl radical recombination, similar to pure methane

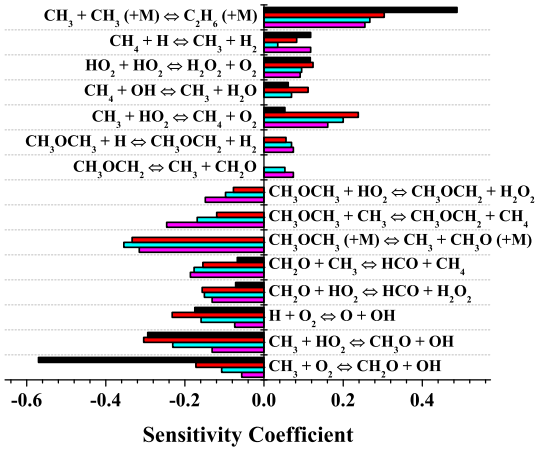

Fig. 21. Sensitivity analyses at 1237 K and ~10 atm. Comparing mixture composition. ■ – CH_4 (9.4 atm), ■ – 80/20 CH_4/DME (7.7 atm), ■ – 60/40 CH_4/DME (7.3 atm), ■ – DME (11.4 atm).

and 80/20 blends. The most-promoting reaction for all equivalence ratios is unimolecular decomposition, $CH_3OCH_3(+M) \rightleftarrows CH_3\dot{O} + \dot{C}H_3(+M)$. Another highly promoting reaction is $CH_3OCH_3 + \dot{C}H_3 \rightleftarrows CH_3O\dot{C}H_2 + CH_4$, highlighting the importance of methyl radical chemistry in DME oxidation at high temperatures.

5.4. Influence of mixture composition

The comparison of the ignition delay times of the four mixture compositions studied is shown in Fig. 20 for pressures of 7–10 atm. This comparison shows that as DME concentration increases, ignition delay time decreases over the whole temperature range of this study. Mech_56.54 predicts all experimental data very well. The mechanism in particular predicts the decrease in ignition delay time as the mixture composition changes.

As has been stated previously, it is the reactions of DME which control ignition of the blends even though there is a greater concentration of methane. This importance of DME concentration shows how the addition of small amounts of DME allows the radical pool to build at lower temperatures and therefore increase the rate of methane combustion. To quantify this effect, at approximately 1361 K in Fig. 20(c) at $\phi = 1.0$ the ignition delay time for pure methane is 884 μs; for 80/20 it is 152 μs; for 60/40 it is 108 μs; and for pure DME it is 59 μs. So ignition delay time is reduced by a factor of 5.8 when just 20% DME is added to methane.

Figure 21 shows sensitivity analyses for different mixture compositions presented in Fig. 20(c) at $\phi = 1.0$ and at 1237 K. Methyl radical recombination is again the most-inhibiting reaction over all mixture compositions, as discussed earlier. As has also been discussed previously, both blends show high sensitivity to reactions involving DME and methyl radicals.

In summary, as the DME concentration increases, the ignition delay times decrease. The addition of DME to methane enhances the reactivity of methane by increasing radical production at low temperature through DME's chain branching pathway, and through its unimolecular decomposition and relatively fast H-atom abstraction rate constants at high temperature.

6. Conclusions

A wide range of new ignition delay time data for pure methane, pure DME, 80/20, and 60/40 mixtures of both fuels in 'air' are presented. Pressures from 7 to 41 atm were studied in the temperature range 600–1600 K. These data allow for mechanism validation under conditions similar to those found in compression ignition engines and gas turbines, where methane and DME have been burned previously. A new detailed chemical kinetic model (Mech_56.54) for the combustion of DME is presented and validated with the new data and data available in literature (Flow reactor; JSR; RCM; shock-tube ignition delay time and shock-tube speciation; flame speeds and flame speciation). The new model utilizes AramcoMech1.3 [41], which had been well-validated previously, and is the first model to incorporate the calculations of Li et al. [63] and Yamada et al. [58]. It is able to predict the pure methane ignition delay times measured and presented here. It was found that, to accurately predict the ignition delay times of DME, the inclusion of a QRRK pressure-dependent treatment of the low-temperature oxidation reactions was important. In particular, the β-scission of the methoxymethyl radical showed significant pressure-dependent fall-off. RRKM/ME calculations were performed to calculate the pressure-dependent rate constants for the β-scission of the methoxymethyl radical.

The rate constants for unimolecular decomposition and H-atom abstractions by a variety of radical species from DME have been adopted from high-accuracy measurements and/or calculations where possible in Mech_56.54. The use of these calculated rate constants and the application of pressure-dependent rate constants for the lower-temperature reactions of DME is an important improvement to its chemical kinetic mechanism. Further investigation into these low-temperature reactions would help to remove any remaining uncertainty in this chemical kinetic model. The new data presented in this paper comprehensively covers a wide range of engine- and combustor-relevant conditions. Validation of the detailed chemical kinetic mechanism under these wide range of conditions presents an important improvement in the understanding of the combustion chemistry of DME due to its dominance in controlling the ignition behavior of its mixtures with methane.

Acknowledgments

Peter O'Toole acknowledges the financial support of the Irish government under PRTLI Cycle 4. Ultan Burke acknowledges the financial support of the Irish Research Council. Kieran P. Somers acknowledges the support of Science Foundation Ireland under Grant No. [08/IN1./I2055] as part of their Principal Investigator Awards. The work conducted at TAMU was funded by Rolls-Royce Canda under the direction of Dr. Gilles Bourque. The help from Nicole Donato and John Pemelton on some of the TAMU experiments and data analysis is appreciated.

Appendix A. Supplementary material

Supplementary data associated with this article can be found, in the online version, at http://dx.doi.org/10.1016/j.combustflame.2014.08.014.

References

[1] A. Molino, F. Nanna, Y. Ding, B. Bikson, G. Braccio, Fuel 103 (2013) 1003–1009.
[2] Y. Adachi, M. Komoto, I. Watanabe, Y. Ohno, K. Fujimoto, Fuel 79 (2000) 229–234.
[3] T.A. Semelsberger, R.L. Borup, H.L. Greene, J. Power Sources 156 (2006) 497–511.
[4] W. Ying, L. Genbao, Z. Wei, Z. Longbao, Fuel Process. Technol. 89 (2008) 1272–1280.
[5] W. Ying, Z. Longbao, Energy Fuels 21 (2007) 1454–1458.
[6] S.C. Sorensen, ASME transactions, J. Eng. Gas Turbines Power 123 (2001) 652–658.
[7] P. Kapus, H. Ofner, Development of Fuel Injection Equipment and Combustion System for DI Diesels Operated on Dimethyl Ether, SAE Technical Paper 950062, 1995.
[8] M.C. Lee, S.B. Seo, J.H. Chung, Y.J. Joo, D.H. Ahn, Fuel 88 (2009) 657–662.
[9] P.A. Glaude, R. Fournet, R. Bounacceur, M. Moliere, DME as a Potential Alternative Fuel for Gas Turbines: A Numerical Approach to Combustion and

Oxidation Kinetics, in: ASME 2011 Turbo Expo: Turbine Technical Conference and Exposition, 2011, pp. 649–658.
[10] M. Konno, Z. Chen, SAE Paper 2005-01-0182, 2005, doi:10.4271/2005-01-0182.
[11] Y. Tsutsumi, K. Hoshina, A. Iijima, H. Shoji, SAE Paper, 2007-32-0041, 2007.
[12] C.A. Daly, J.M. Simmie, J. Würmel, N. Djebaĭli, C. Paillard, Combust. Flame 125 (2001) 1329–1340.
[13] Z. Zhao, A. Kazakov, F.L. Dryer, Combust. Flame 139 (2004) 52–60.
[14] X.L. Zheng, T.F. Lu, C.K. Law, C.K. Westbrook, H.J. Curran, Proc. Combust. Inst. 30 (2005) 1101–1109.
[15] X. Qin, Y. Ju, Proc. Combust. Inst. 30 (2005) 233–240.
[16] Y.L. Wang, A.T. Holley, C. Ji, F.N. Egolfopoulos, T.T. Tsotsis, H.J. Curran, Proc. Combust. Inst. 32 (2009) 1035–1042.
[17] J. de Vries, W.B. Lowry, Z. Serinyel, H.J. Curran, E.L. Petersen, Fuel 90 (2011) 331–338.
[18] P. Dagaut, C. Daly, J.M. Simmie, M. Cathonnet, Proc. Combust. Inst. 27 (1998) 361–369.
[19] S.L. Fischer, F.L. Dryer, H.J. Curran, Int. J. Chem. Kinet. 32 (2000) 713–740.
[20] H.J. Curran, S.L. Fischer, F.L. Dryer, Int. J. Chem. Kinet. 32 (2000) 741–759.
[21] Z. Zhao, M. Chaos, A. Kazakov, F.L. Dryer, Int. J. Chem. Kinet. 40 (2008) 1–18.
[22] J. Wang, M. Chaos, B. Yang, T.A. Cool, F.L. Dryer, T. Kasper, N. Hansen, K. Kohse-Hoinghaus, P.R. Westmoreland, Phys. Chem. Chem. Phys. 11 (2009) 1328–1339.
[23] T.A. Cool, J. Wang, N. Hansen, P.R. Westmoreland, F.L. Dryer, Z. Zhao, A. Kazakov, T. Kasper, K. Kohse-Höinghaus, Proc. Combust. Inst. 31 (2007) 285–293.
[24] R.D. Cook, D.F. Davidson, R.K. Hanson, J. Phys. Chem. A 113 (2009) 9974–9980.
[25] S.H. Pyun, W. Ren, K.-Y. Lam, D.F. Davidson, R.K. Hanson, Combust. Flame 160 (2013) 747–754.
[26] L.J. Spadaccini, M.B. Colket Iii, Prog. Energy Combust. Sci. 20 (1994) 431–460.
[27] T. Tsuboi, H.G. Wagner, Proc. Combust. Inst. 15 (1975) 883–890.
[28] E.L. Petersen, M. Röhrig, D.F. Davidson, R.K. Hanson, C.T. Bowman, Proc. Combust. Inst. 26 (1996) 799–806.
[29] E.L. Petersen, D.F. Davidson, R.K. Hanson, Combust. Flame 117 (1999) 272–290.
[30] E.L. Petersen, D.F. Davidson, R.K. Hanson, J. Prop. Power 15 (1999) 82–91.
[31] L. Brett, J. Macnamara, P. Musch, J.M. Simmie, Combust. Flame 124 (2001) 326–329.
[32] V.P. Zhukov, V.A. Sechenov, A.Y. Starikovskii, Combust. Expl. Shock Waves 30 (2003) 487–495.
[33] J. Huang, P.G. Hill, W.K. Bushe, S.R. Munshi, Combust. Flame 136 (2004) 25–42.
[34] G. Mittal, M. Chaos, C.-J. Sung, F.L. Dryer, Fuel Proc. Tech. 89 (2008) 1244–1254.
[35] U. Pfahl, K. Fieweger, G. Adomeit, Proc. Combust. Inst. 26 (1996) 781–789.
[36] R.D. Cook, D.F. Davidson, R.K. Hanson, Proc. Combust. Inst. 32 (2009) 189–196.
[37] C. Tang, L. Wei, J. Zhang, X. Man, Z. Huang, Energy Fuels 26 (2012) 6720–6728.
[38] D. Liu, J. Santner, C. Togbé, D. Felsmann, J. Koppmann, A. Lackner, X. Yang, X. Shen, Y. Ju, K. Kohse-Höinghaus, Combust. Flame 160 (2013) 2654–2668.
[39] H. Guo, W. Sun, F.M. Haas, T. Farouk, F.L. Dryer, Y. Ju, Proc. Combust. Inst. 34 (2013) 573–581.
[40] F. Herrmann, B. Jochim, P. Oßwald, L. Cai, H. Pitsch, K. Kohse-Höinghaus, Combust. Flame 161 (2014) 384–397.
[41] W.K. Metcalfe, S.M. Burke, S.S. Ahmed, H.J. Curran, Int. J. Chem. Kinet. 45 (2013) 638–675.
[42] W.S. Affleck, A. Thomas, Proc. Inst. Mech. Eng. 183 (1969) 365–385.
[43] D. Darcy, H. Nakamura, C.J. Tobin, M. Mehl, W.K. Metcalfe, W.J. Pitz, C.K. Westbrook, H.J. Curran, Combust. Flame 161 (2014) 65–74.
[44] C. Morley, GasEq, Version 0.76, 2004, <http://www.gaseq.co.uk>.
[45] D. Darcy, C.J. Tobin, K. Yasunaga, J.M. Simmie, J. Würmel, W.K. Metcalfe, T. Niass, S.S. Ahmed, C.K. Westbrook, H.J. Curran, Combust. Flame 159 (2012) 2219–2232.
[46] E.L. Petersen, M.J.A. Rickard, M.W. Crofton, E.D. Abbey, M.J. Traum, D.M. Kalitan, Meas. Sci. Technol. 16 (2005) 1716–1729.
[47] C.J. Aul, W.K. Metcalfe, S.M. Burke, H.J. Curran, E.L. Petersen, Combust. Flame 160 (2013) 1153–1167.
[48] E.L. Petersen, R.K. Hanson, Shock Waves 10 (2001) 405–420.
[49] C.M. Zinner, Methane and Dimethyl Ether Oxidation at Elevated Temperatures and Pressure, M.Sc. Thesis, Univ. of Central Florida, USA, 2006.
[50] J. Pemelton, N. Marquet, W. Metcalfe, H.J. Curran, E.L. Petersen, 7th US Natl. Tech. Meet. Combust. Inst., Atlanta, GA, 2011.
[51] CHEMKIN-PRO 15112, Reaction Design: San Diego, 2011.
[52] J. Würmel, Detailed Chemical Kinetics Combined with a Computational Fluid Dynamics Study of a Twin Piston Rapid Compression Machine, PhD Thesis, Dept. Chem., Natl. Univ. Ireland Galway, Ireland, 2004.
[53] E.L. Petersen, A Shock Tube and Diagnostics for Chemistry Measurements at Elevated Pressures with Application to Methane Ignition, Ph.D. Thesis, Dept. of Mech. Eng., Stanford Univ., USA, 1998.
[54] A. Kéromnès, W.K. Metcalfe, K.A. Heufer, N. Donohoe, A.K. Das, C.-J. Sung, J. Herzler, C. Naumann, P. Griebel, O. Mathieu, M.C. Krejci, E.L. Petersen, W.J. Pitz, H.J. Curran, Combust. Flame 160 (2013) 995–1011.
[55] S.M. Burke, W. Metcalfe, O. Herbinet, F. Battin-Leclerc, F.M. Haas, J. Santner, F.L. Dryer, H.J. Curran, Combust. Flame 161 (11) (2014) 2765–2784.
[56] E.R. Ritter, J.W. Bozzelli, Int. J. Chem. Kinet. 23 (1991) 767–778.
[57] S.M. Burke, Development of a Chemical Kinetic Mechanism for Small Hydrocarbons, PhD thesis, Dept. Chem., Natl. Univ. Ireland Galway, Ireland, 2013.
[58] T. Yamada, J.W. Bozzelli, T.H. Lay, Int. J. Chem. Kinet. 32 (2000) 435–452.
[59] J. Mendes, C.-W. Zhou, H.J. Curran, J. Phys. Chem. A 118 (2014) 1300–1308.
[60] H.-H. Carstensen, A.M. Dean, Proc. Combust. Inst. 30 (2005) 995–1003.
[61] TR.S. Tranter, P.T. Lynch, C.J. Annesley, J. Phys. Chem. A 116 (2012) 7287–7292.
[62] A.Y. Chang, J.W. Bozzelli, A.M. Dean, Z. Phys. Chem. 214 (2000) 1533–1568.
[63] Q.S. Li, Y. Zhang, S. Zhang, J. Phys. Chem. A 108 (2004) 2014–2019.
[64] J.A. Miller, S.J. Klippenstein, J. Phys. Chem. A 117 (2013) 2718–2727.
[65] C.F. Goldsmith, W.H. Green, S.J. Klippenstein, J. Phys. Chem. A 116 (2012) 3325–3346.
[66] M.E.C.R.J. Kee, P. Glarborg, Chemically Reacting Flow Theory and Practice, 1st ed., John Wiley and Son, Inc., New Jersey, 2003.
[67] W.M. Haynes, Critical Constants of Organic Compounds, in: CRC Handbook of Chemistry and Physics, 91st ed., CRC Press, Boca Raton, Florida.
[68] A.W. Jasper, J.A. Miller, Combust. Flame 161 (1) (2014) 101–110.
[69] J.A. Montgomery, M.J. Frisch, J.W. Ochterski, G.A. Petersson, J. Chem. Phys. 112 (2000) 6532–6542.
[70] J.W. Ochterski, G.A. Petersson, J.A. Montgomery, J. Chem. Phys. 104 (1996) 2598–2619.
[71] L.A. Curtiss, K. Raghavachari, P.C. Redfern, V. Rassolov, J.A. Pople, J. Chem. Phys. 109 (1998) 7764–7776.
[72] A.D. Becke, J. Chem. Phys. 98 (1993) 5648–5652.
[73] C. Lee, W. Yang, R.G. Parr, Phys. Rev. B 37 (1988) 785–789.
[74] Gaussian 09, Revision C.01, M.J. Frisch, G.W. Trucks, H.B. Schlegel, G.E. Scuseria, M.A. Robb, J.R. Cheeseman, J.A. Montgomery, Jr., T. Vreven, K.N. Kudin, J. C. Burant, J. M. Millam, S. S. Iyengar, J. Tomasi, V. Barone, B. Mennucci, M. Cossi, G. Scalmani, N. Rega, G.A. Petersson, H. Nakatsuji, M. Hada, M. Ehara, K. Toyota, R. Fukuda, J. Hasegawa, M. Ishida, T. Nakajima, Y. Honda, O. Kitao, H. Nakai, M. Klene, X. Li, J.E. Knox, H.P. Hratchian, J.B. Cross, V. Bakken, C. Adamo, J. Jaramillo, R. Gomperts, R.E. Stratmann, O. Yazyev, A.J. Austin, R. Cammi, C. Pomelli, J.W. Ochterski, P.Y. Ayala, K. Morokuma, G.A. Voth, P. Salvador, J.J. Dannenberg, V.G. Zakrzewski, S. Dapprich, A.D. Daniels, M.C. Strain, O. Farkas, D.K. Malick, A.D. Rabuck, K. Raghavachari, J.B. Foresman, J.V. Ortiz, Q. Cui, A.G. Baboul, S. Clifford, J. Cioslowski, B.B. Stefanov, G. Liu, A. Liashenko, P. Piskorz, I. Komaromi, R.L. Martin, D.J. Fox, T. Keith, M.A. Al-Laham, C.Y. Peng, A. Nanayakkara, M. Challacombe, P.M.W. Gill, B. Johnson, W. Chen, M.W. Wong, C. Gonzalez, J.A. Pople, Gaussian, Inc., Wallingford CT, 2004.
[75] V. Mokrushin, W. Tsang, ChemRate version 1.5.8, NIST, Gaithersburg, MD 20899. <http://mokrushin.com/ChemRate/chemrate.html> (accessed 21.06.13).
[76] K.A. Sahetchian, R. Rigny, J. Tardieu de Maleissye, L. Batt, M. Anwar Khan, S. Mathews, Sym. (Int.) Combust. 24 (1992) 637–643.